Calcite fabric development in calc-mylonite during progressive shallowing of a shear zone: An example from the South Tibetan Detachment system (Kali Gandaki valley, Central Himalaya)

DOI:10.1016/j.tecto.2023.230176

Tectonophysics

Calcite fabric development in calc-mylonite during progressive shallowing of a shear zone: an example from the Annapurna Detachment zone (central Himalaya, Western Nepal)

--Manuscript Draft--

Manuscript Number:	
Article Type:	Research Paper
Keywords:	Calcite crystallographic preferred orientation; paleopiezometry; kinematic vorticity; Himalaya; South Tibetan Detachment System
Corresponding Author:	Chiara Montomoli University of Turin ITALY
First Author:	Laura Nania, PhD
Order of Authors:	Laura Nania, PhD
	Chiara Montomoli, PhD
	Salvatore Iaccarino, PhD
	Rodolfo Carosi, PhD
Abstract:	Calcite-rich lithologies within the Annapurna Detachment zone in central Himalaya (Kali Gandaki region, Western Nepal) have been characterized for the superimposition of microstructures to unravel deformation variations during syn-collisional exhumation. Finite-strain, grain size, twinning, and crystallographic preferred orientations have been combined to define the contribution of dynamic recrystallization and twinning in calcite in the overall deformation. Dynamic recrystallization and twinning occurred respectively at temperatures of c. 400-550°C and <250°C. The comparison of calcite-based paleopiezometers indicates that cooling occurred along with an increase in differential stress from c. 4-19 MPa up to c. 118-154 MPa at decreasing strain rates. Flow estimates with the subsimple shear (30-50% of simple shear) regime for both fabrics support a single progressive deformation where the plastic regime progressively changed. We interpret the changes in intracrystalline deformation mechanisms in calcite and their differences in differential stress records, deformation temperature, and strain rate as linked to the exhumation of the rocks induced by the detachment, from deeper to upper crustal levels. Results for the Annapurna Detachment zone have been compared with the literature database for the area and for its regional prosecution in Himalaya, the South Tibetan Detachment System. This study highlights how variations in lithology in regional-scale shear zones influences the exhumation path and the overall architecture of the shear zone itself.
Suggested Reviewers:	Eugenio Fazio, PhD Associate Professor, University of Catania efazio@unict.it He is an expert for CPO methodology and meso and micro structural geology
	Richard D Law, PhD Full Professor, University of Virginia Tech rdlaw@vt.edu Expert in Himalayan Geology, meso and microstructural analysis, South Tibetan Detachment System, crystallographic preferred orientation
	Jean-Luc Epard, PhD Associate Professor, University of Lausanne Institute of Earth Sciences Jean-Luc.Epard@unil.ch Expert in Himalayan Geology snd structural geology
	Sean Long Associate Professor, Washington State University sean.p.long@wsu.edu Expert of himalyan geology, South Tibetan Detachment System, microstructures

Calcite-rich lithologies within the Annapurna Detachment zone in central Himalaya (Kali Gandaki region, Western Nepal) have been characterized for the superimposition of microstructures to unravel deformation variations during syn-collisional exhumation. Finite-strain, grain size, twinning, and crystallographic preferred orientations have been combined to define the contribution of dynamic recrystallization and twinning in calcite in the overall deformation. Dynamic recrystallization and twinning occurred respectively at temperatures of c. 400-550°C and <250°C. The comparison of calcite-based paleopiezometers indicates that cooling occurred along with an increase in differential stress from c. 4-19 MPa up to c. 118-154 MPa at decreasing strain rates. Flow estimates with the subsimple shear (30-50% of simple shear) regime for both fabrics support a single progressive deformation where the plastic regime progressively changed. We interpret the changes in intracrystalline deformation mechanisms in calcite and their differences in differential stress records, deformation temperature, and strain rate as linked to the exhumation of the rocks induced by the detachment, from deeper to upper crustal levels. Results for the Annapurna Detachment zone have been compared with the literature database for the area and for its regional prosecution in Himalaya, the South Tibetan Detachment System. This study highlights how variations in lithology in regional-scale shear zones influences the exhumation path and the overall architecture of the shear zone itself.

Highlights

- Calcite fabrics superimposition can record crustal exhumation paths in shear zones
- Shallowing through progressive stages of ductile slip on the Annapurna Detachment
- Protracted ductile shearing results in a lack of a brittle South Tibetan detachment
- Lithologies variation over the Himalayan strike influences the overall architecture

Calcite fabric development in calc-mylonite during progressive shallowing of a shear zone: an example from the Annapurna Detachment zone (central Himalaya, Western Nepal)

Laura Nania [a,b], Chiara Montomoli [c,d,*] Salvatore Iaccarino [c], Rodolfo Carosi [c]

a. Dipartimento di Scienze della Terra, Università di Firenze, Via Giorgio la Pira, 4, 50121, Firenze, Italy
b. Geological Survey of Canada, Natural Resources Canada, 601 Booth St, Ottawa, ON, K1A 0E8, Canada
c. Dipartimento di Scienze della Terra, Università di Torino, via Valperga Caluso, 35, 10125 Torino, Italy
d. Istituto di Geoscienze e Georisorse, CNR, Via Giuseppe Moruzzi, 1, 56127, Pisa, Italy

L.N., laura.nania@nrcan-rncan.gc.ca; C.M., chiara.montomoli@unito.it; S.I., salvatore.iaccarino@unito.it; R.C., rodolfo.carosi@unito.it

Corresponding author: Chiara Montomoli, chiara.montomoli@unito.it

Highlights

- Calcite fabrics superimposition can record crustal exhumation paths in shear zones
- Shallowing through progressive stages of ductile slip on the Annapurna Detachment
- Protracted ductile shearing results in a lack of a brittle South Tibetan detachment
- Lithologies variation over the Himalayan strike influences the overall architecture

Abstract

Calcite-rich lithologies within the Annapurna Detachment zone in central Himalaya (Kali Gandaki region, Western Nepal) have been characterized for the superimposition of microstructures to unravel deformation variations during syn-collisional exhumation. Finite-strain, grain size, twinning, and crystallographic preferred orientations have been combined to define the contribution of dynamic recrystallization and twinning in calcite in the overall deformation. Dynamic recrystallization and twinning occurred respectively at temperatures of c. 400-550°C and <250°C. The comparison of calcite-based paleopiezometers indicates that cooling occurred along with an increase in differential stress from c. 4-19 MPa up to c. 118-154 MPa at decreasing strain rates. Flow estimates with the subsimple shear (30-50% of simple shear) regime for both fabrics support a single progressive deformation where

the plastic regime progressively changed. We interpret the changes in intracrystalline deformation mechanisms in calcite and their differences in differential stress records, deformation temperature, and strain rate as linked to the exhumation of the rocks induced by the detachment, from deeper to upper crustal levels. Results for the Annapurna Detachment zone have been compared with the literature database for the area and for its regional prosecution in Himalaya, the South Tibetan Detachment System. This study highlights how variations in lithology in regional-scale shear zones influences the exhumation path and the overall architecture of the shear zone itself.

Keywords: Calcite crystallographic preferred orientation, paleopiezometry, kinematic vorticity, Himalaya, South Tibetan Detachment System.

1. Introduction

Regional scale, orogenic wide, shear zones are regions of the Earth's crust that strongly affect orogens architecture through time. In the lower to the mid-upper continental crust, deformation often results in mylonitic zones of variable width, depending on intrinsic and extrinsic (regional) deformation parameters (e.g., see Ebert et al., 2008, 2009; Hunter et al., 2019; Cawood and Platt, 2021; Daczko and Piazolo, 2022 with references). When marbles and carbonate-rich rocks are involved, meso-structural analysis can be a non-easy task (Nania et al., 2022b). The low contrast in competence between rheological domains (e.g., primary or secondary foliations, see Passchier and Trouw, 2005) and the small occurrences of micas in marbles prevent the formation of clear structures and kinematic indicators typically used for a first characterization of the shear zones. To characterize the deformation of calc-mylonites, it is required to integrate mesostructural observations with microstructural analysis (e.g., Molli and Heilbronner, 1999; Molli et al., 2000; Leiss and Molli, 2003; Ebert et al., 2007; Oesterling et al., 2007; Herwegh et al., 2008; Molli et al., 2011; Rogowitz et al., 2014; Spanos et al., 2015; Sarkarinejad and Heibati, 2017; Bauer et al., 2018; Negrini et al., 2018; Lacombe et al., 2021; Nania et al., 2022b). However, given the difficulty of describing the mylonitic fabric at the mesoscale in marbles, there are few works that engage in their study for tectonic investigations, and marble mylonites are still under-researched.

An example of this issue can be addressed in the case of the South Tibetan Detachment System (STDS) in Himalaya. The STDS is a regional, syn-collisional, normal faults system, which has been largely the focus, over the last forty years, to define tectonic models for the exhumation of mid-crustal rocks in collisional settings (Burg et al., 1983; Burchfiel and Royden, 1985; Hodges et al., 1992; Grujic et al., 1996; Carosi et al., 1998; Beaumont et al., 2001, 2004; Vannay and Grasemann, 2001; Godin et al., 2006; Webb et al., 2007; Kohn, 2008; Larson et al., 2015; Iaccarino et al., 2017). The STDS laterally involves different regions of the Himalaya and, therefore, different lithotypes. Nonetheless, most of the tectonic (including microtectonics) studies on STDS mostly concern areas where quartz-bearing rocks constitute the main involved lithotypes, with minor attempts on calcite-rich tectonites in Central Himalaya (Parsons et al., 2016b, 2016d). Particularly in the Everest area, where spectacular outcrops of both quartz-rich and carbonate-rich rocks are described (Carosi et al., 1998, 2002; Searle et al., 2003; Law et al., 2004, 2011; Waters et al., 2019), mesoscale observation, microstructure analysis, and geochronological investigation have been adopted mainly on quartz-rich tectonites to define the picture of the detachment system (Waters et al., 2019 with references), with fewer characterization of the carbonate lithotypes in uppermost sections (Carosi et al., 1998; Corthouts et al., 2016; Larson et al., 2020). There, the STDS is made up by (1) an older lower mylonitic zone, affecting mid-crustal rocks in the footwall (essentially quartz-bearing lithologies) and marine metasediments in the hanging wall, and (2) an upper younger discrete brittle fault, within the upward carbonate marine metasediments, with the same kinematic and sense of shear of the lower detachment to which it laterally rejoints (Carosi et al., 1998; Searle, 1999; Searle et al., 2003; Law et al., 2004, 2011; Waters et al., 2019; Kellett et al., 2019; Larson et al., 2020). The discrete upper younger brittle fault, however, is not documented in several areas along the Himalaya (e.g., Cottle et al., 2007; Carosi et al., 2002, 2013; Kellett et al., 2019, with references), e.g., when the km-thick mylonitic detachment involves carbonate-rich rocks (Nania et al., 2022b). Consequently, how the two elements of the STDS are related to a regional scale is still under debate (Cottle et al., 2011; Carosi et al., 2013, 2018; Montomoli et al., 2017; Kellett et al., 2019, with references therein; Nania et al., 2022b). It is therefore crucial to define how is the overall deformation of the detachment system recorded in other areas of the belt, where lithotypes different from quartz-rich rocks, such as marble mylonite, are involved.

This is the reason why we decided to characterize the STDS in a well-known region, the Kali Gandaki valley (Central Nepal, Fig. 1; Fuchs and Frank, 1970), where the calcite fabric of marble mylonites (the main lithology) has been only little investigated until now (e.g., Parsons et al., 2016b, 2016d). The ductile shear zone in the Kali Gandaki valley is known as Annapurna Detachment (Fig. 2a, b; Vannay and Hodges, 1996; Godin et al., 1999a; Godin, 2003; Waters, 2019; Pye et al., 2022, with references) hereafter named as Annapurna Detachment zone. Marbles and limestones in the study area are spectacularly exposed (Colchen et al., 1986; Burchfiel et al., 1992, with references; Vannay and Hodges, 1996; Godin et al., 1999a; Searle, 2010, with references; Parsons et al., 2016b, 2016c, 2016d) but only few kinematic indicators occur (e.g., Carosi et al., 2014; Parsons et al., 2016b, 2016d). We, therefore, integrated optical, crystallographic preferred orientation (CPO), and image analyses to identify new kinematic indicators and to define the mylonitic fabric and the relative contribution and timing of the microstructures development in the deformation regimes. We particularly focused on the type of the flow, the kinematic vorticity conditions, and the strain rate. This allowed us not only to define the deformation evolution of the local Annapurna Detachment zone in the Kali Gandaki area, but also to compare different exhumation styles of the STDS for different and similar lithotypes along the belt and provides new insights into a more general perspective concerning strain variation in marble mylonite during shear zones evolution.

2. Geological setting

2.1. Geological overview of the Himalaya

The Himalaya is an active collisional orogen linked to the collision and indentation of the Indian Plate into the Eurasia Plate started at c. 59-61 Ma (Hu et al., 2016; Parsons et al., 2020; An et al., 2021). From south to north, the main km-thick litho-tectonics units, accreted from the Indian northern margin, are (Fig. 1; see Hodges, 2000 for a review): the Siwalik Group (or Subhimalayan Sequence, consisting of

Tertiary molasse sediments), the Lesser Himalayan Sequence (LHS) (subgreenschist facies to low-amphibolite facies rocks), the Greater Himalayan Sequence (GHS) (greenschist to high-temperature amphibolite facies rocks), and the Tethyan Himalayan Sequences (THS) (upper greenschist facies metamorphic rock to unmetamorphosed sedimentary rocks).

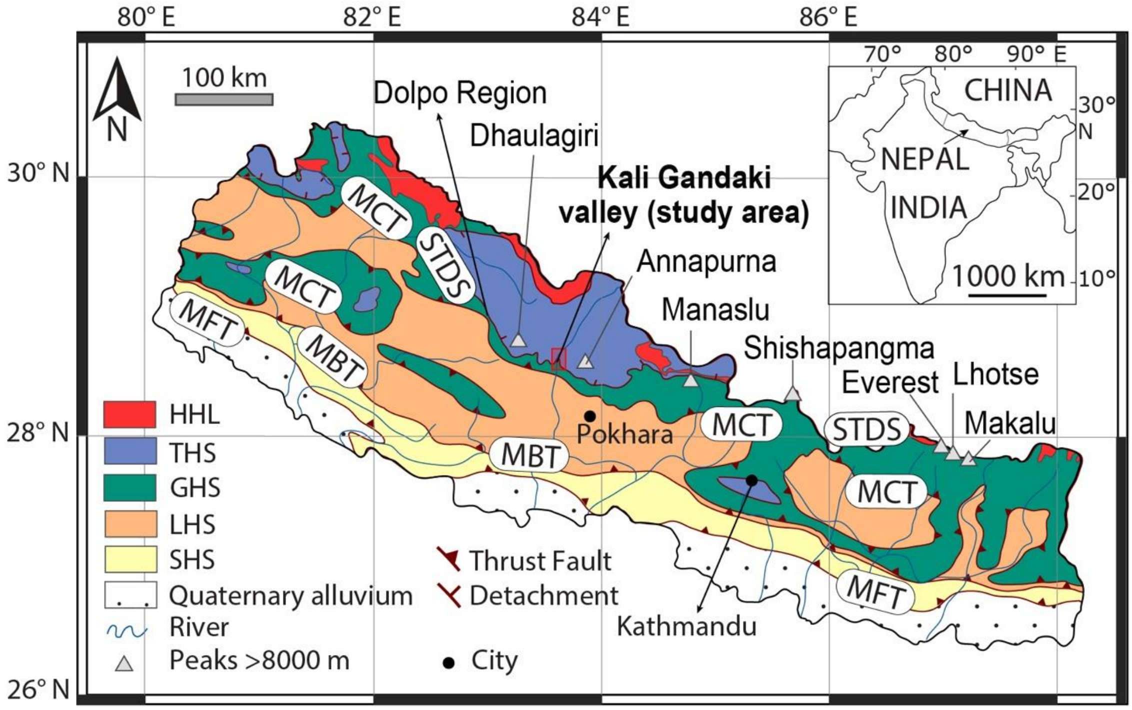

Figure 1

The GHS and the THS have undergone two main tectonic stages: (1) the main collision in the Eocene, and (2) a (syn-collisional) southward exhumation (namely N–S extension) of the north-dipping units in the Late Oligocene-Miocene, characterized by nearly isothermal decompression followed by retrogression (Hodges, 2000, with references). During the southward exhumation, the regional-scale STDS juxtaposed the high-grade rocks of the GHS in the footwall against the low-grade metasediments of the THS in the hanging-wall (Caby et al., 1983; Burg and Chen, 1984; Burchfiel et al., 1992; Carosi et al., 1998; Law et al., 2011; Iaccarino et al., 2017; Montomoli et al., 2017; Kellett et al., 2019, with references). Especially in the northern part of the Himalaya, corresponding to the northern THS (i.e., see the geographical/topographic division of Yin, 2006), and to a lesser extent at the top of the GHS, the collisional tectonics resulted in crustal thinning through orogen-parallel E-W extension (Jessup et al., 2019; Larson et al., 2019; Pye et al., 2022, with references). The tectonic shift from N-S to E-W extension occurred from the late Miocene (Nagy et al., 2015; Parsons et al., 2016a; Larson et al., 2019), and was probably a progressive tectonic style changes occurred overtime after the end of the STDS activity (Murphy et al., 2002; Chen et al., 2022, with references; Pye et al., 2022). The E-W extension developed through N-S trending normal faults/grabens (Coleman, 1996; Colchen, 1999; Blisniuk et al., 2001; Jessup et al., 2008, 2019; Mitsuishi et al., 2012; Larson et al., 2019) and a possible generalized re-heating and thermal relaxation (Nania et al., 2022a) along with granitic intrusions in several areas (Roger et al., 1995; Visonà and Lombardo, 2002; Streule et al., 2010; Mitsuishi et al., 2012; Visonà et al., 2012; Carosi et al., 2013; Zhang et al., 2020; Chen et al., 2022). From the late Miocene-Pliocene, especially in the southern part of the belt, the Himalayan exhumation rate abruptly increased together with the extreme climate-induced erosion rates (Huntington et al., 2006; Garzanti et al., 2007; Gemignani et al., 2018; Govin et al., 2020). In the Thakkhola region of Western Nepal, this tectonic and climate-induced landscape modelling resulted into the Kali Gandaki valley (Fig. 1; Fig. 2a), a deep N-S gorge carved normal to the Himalayan trend (Colchen et al., 1986; Carosi et al., 2014).

2.2. The upper Kali Gandaki valley

The upper Kali Gandaki valley, shown in Fig. 2a, exposes the crystalline rocks of the GHS and the nearly continuous sequence of the THS along a natural and almost N-S trending cross-section (Colchen et al., 1980; Vannay and Hodges, 1996; Godin et al., 1999a; Godin, 2003; Carosi et al., 2014; Parsons et al., 2016c). Over the last years, the GHS exhumation in the Kali Gandaki valley has been recognized as composite and diachronous for (at least) two main portions, divided by high-temperature tectono-metamorphic discontinuities (e.g., the Kalopani shear zone, Fig. 2a, Carosi et al., 2014, 2016; and the High Himalayan Discontinuity (HHD), Iaccarino et al., 2015). Hereafter, we define the GHS as made by two sub-units: a lower GHS (GHS_L) and an upper GHS (GHS_U). The GHS_U is the only represented in Fig. 2 and comprises the Units (once referred as Formations by Godin, 2003) II and III distinguished by Godin (2003) and Searle (2010). Unit II is made by calc-silicate bearing gneiss and marble (Fig. 2a, b).

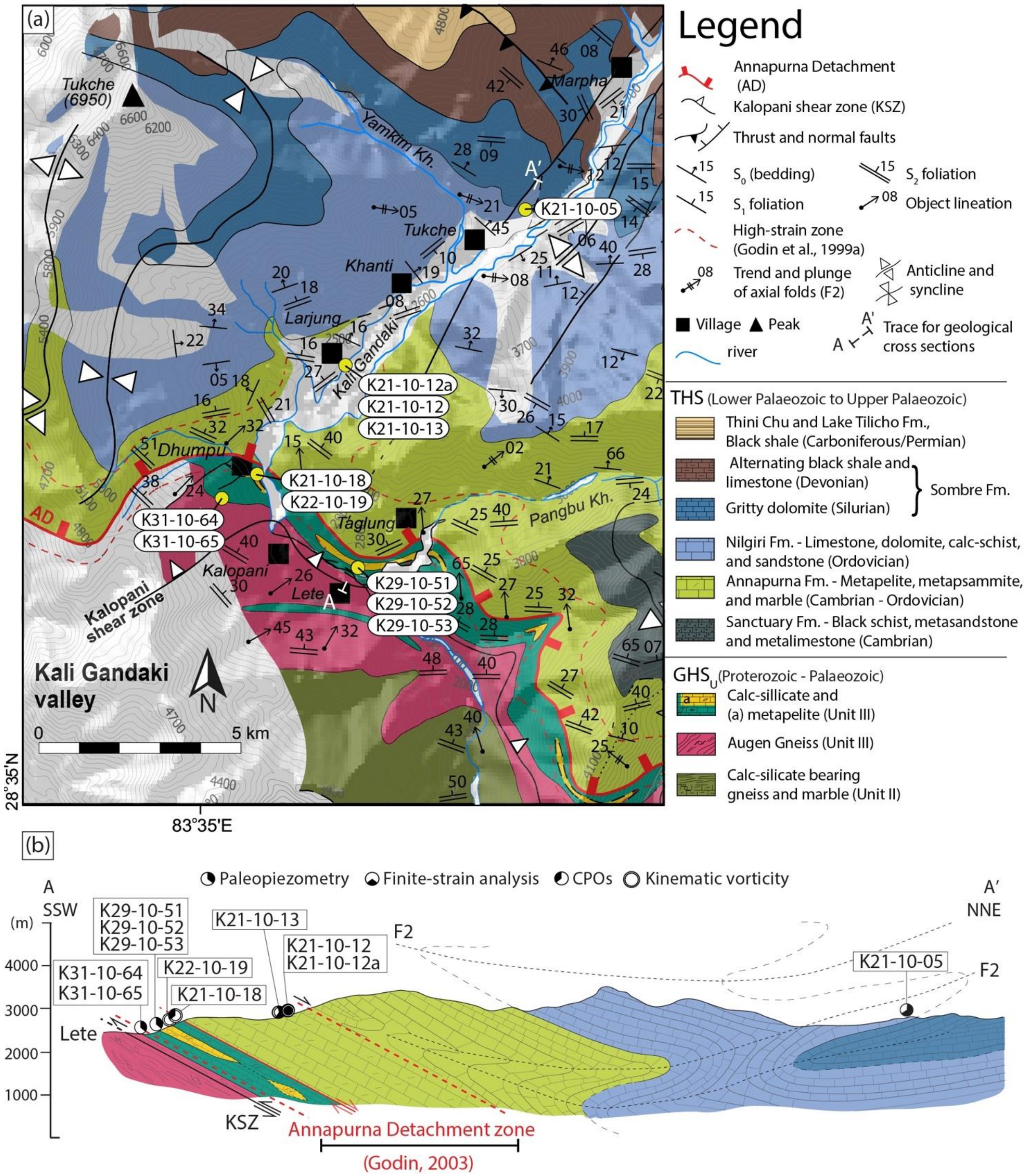

Figure2

The upper portion of GHS$_U$ (Formation III of Godin, 2003 and Unit III, IV and V of Searle, 2010) is made by augen gneiss at the bottom, deformed by the top-to-the-S Kalopani shear Zone (41-36 Ma: Carosi et al., 2016), followed by calc-silicate at the top involved in the Annapurna Detachment zone Fig. 2; Pye et al., 2022, with references). It consists of garnet-tourmaline-bearing augen gneiss, rare foliated two-mica leucogranite, small lenses of kyanite-bearing metapelite, and kyanite-bearing migmatite (Brown and Nazarchuk, 1993; Vannay and Hodges, 1996; Carosi et al., 2016; Parsons et al., 2016c, 2016d). The portions of the GHS_U mainly involved in the detachment are those at the top, consisting of metapelite, white marble, and a 200 m-thick sequence of calc-silicate marble (Fig. 2; see also Brown and Nazarchuk, 1993; Coleman, 1996; Hodges et al., 1996; Vannay and Hodges, 1996; Godin et al., 1999a; Searle, 2010). Coarse-grained marbles have a mineral assemblage of Cal+Qz+Bt+Ms+Kfs (Table 1; mineral abbreviations after Whitney and Evans, 2010), where minor Cpx+Grt+Ves, Cpx+Scp, and Hbl±Grt associations point out upper amphibolite facies metamorphic condition (Vannay and Hodges, 1996; Parsons et al., 2016b, 2016d).

The THS base comprises the highly deformed Sanctuary Fm. (Pêcher, 1978), consisting of Proterozoic/Cambrian black schist, metasandstone, and metalimestone, located in the core of large anticlinal fold nappe (e.g., Fang Antiform) (Fig. 2a, Bordet et al., 1971; Colchen et al., 1986; Hodges et al., 1996; Vannay and Hodges, 1996). The Annapurna Fm. is composed by 1000-1300 m of Cambrian coarse-grained marble and impure metalimestone (Fig. 2), with calcareous meta-psammite and metapelite interbedded with phyllite (Pêcher, 1978; Hodges et al., 1996; Vannay and Hodges, 1996; Godin et al., 1999a, 2001; Godin, 2003; Crouzet et al., 2007; Searle, 2010; Parsons et al., 2016c). A mineral assemblage of Cal+Qz+Ms+Bt±Ep defines a greenschist-facies within the biotite-zone for these rocks (Table 1; Carosi et al., 2014; Parsons et al., 2016b, 2016d). Upward, the Nilgiri Fm., consists of Ordovician micritic metalimestone (Bordet et al., 1971) with a main Cal+Qz+Ms low grade mineral assemblage (Table 1). The Nilgiri Fm. grades to the north into pink dolomitic sandstone and arenite ("North Face quartzites" in Godin, 1999a). The Palaeozoic sequence of the THS continues with lower greenschist/sub-greenschist facies (Crouzet et al., 2007) Silurian-Devonian Sombre Fm., comprehensive of black shale, limestone and arenaceous sandstone, capped by the Permian-Carboniferous Tilicho Lake Fm. and Thini Chu Fm. (Fig. 2a, Garzanti and Pagni Frette, 1991). A continuous Mesozoic to Cenozoic (Eocene) metasedimentary to unmetamorphosed marine succession defines the upper portion of the THS (Bordet et al., 1971; Colchen et al., 1980, 1986; Gradstein et al., 1991; Garzanti et al., 1994).

Within both the GHS_U and the THS a poly-phase tectonic history has been documented (Brown and Nazarchuk, 1993; Hodges et al., 1996; Vannay and Hodges, 1996; Godin, 2003; Parsons et al., 2016b). Due to the lithological and rheological differences between each formation, and to the different structural/crustal level position, the deformation history and the P-T conditions of deformation varies from the GHS_U to the THS (Godin, 2003, with references). Specifically, five deformational events have been ascribed to the THS (Godin, 2003, with references): the D1, corresponding to the collisional tectonic phase (with SW-verging isoclinal folds); the D2 phase for NE-verging folds; the Annapurna Detachment shearing events (defined as D3 and Dt for the ductile extensional transposition onset and the related high-strain zone development, respectively); the D4 for the post-peak metamorphic, associated to southwest-verging kink folds; and the D5 event, linked to the orogen- parallel E-W extension locally recorded by the N-S trending Thakkhola graben and related system of normal faults. In this work, we recognized these deformation stages as three main events consistently with the main tectonic phases of collision, N–S extension, and orogen-parallel E-W extension (described by Vannay and Hodges, 1996), resulting in the most evident structures in the study area (see Fig. 2). Hereafter, the D2 phase indicates the tectonic stage responsible for the northeast-verging folding in the THS and in the syn (to immediately later) >1500 m-thick ductile high-strain zone of the Annapurna Detachment zone (Fig. 2), grouping the D2, D3 and Dt phases of Godin et al. (1999a, 1999b, 2001). An example of a F2 structure is the Nilgiri anticline, refolding the older Fang Antiform (Colchen et al., 1986; Godin, 2003). We suggest that the axial plane of the dominant F2 northeast-verging mega-folds tends to parallelism with the mylonitic foliation of the Annapurna Detachment zone, being dragged by the detachment movement (Fig. 2b) as originally proposed by Burchfiel et al. (1992). We include in the Annapurna Detachment zone both the ductile "Annapurna detachment" in *sensu strictu* of Godin et al. (1999a) and the "Dhumpu detachment" recently described by Pye et al., (2022).

3. Methods

3.1. Calcite microstructure, paleopiezometry and finite strain analyses

Structural analysis was conducted on an almost N-S transect, oriented normal to the Annapurna Detachment strike (Fig. 2a, b; Fig. 3). We selected eleven field-oriented marble samples from different structural levels: ten specimens within the Annapurna Detachment zone and one immediately above it, in the Nilgiri Fm. for comparison (Fig. 2, Table 1). Standard thin sections were prepared on slides parallel to the mineral lineation and perpendicular to the main foliation for microstructural analysis. Of these, six specimens from the GHS_U, three from the Annapurna Fm., and one from the Nilgiri Fm. were selected for image analysis to quantify the calcite volumetric abundance, aspect ratio, and grain size (see Table 1, Table 2). Large areas of interconnected calcite crystals were selected for each specimen to obtain a representative sample of the microstructure. For each area, multiple images with the same pixel size resolution of 5.08 μm (at least four different images for each area, rotated of 45°) were acquired under cross-polarized light with and without the gypsum plate inserted, to unambiguously identify calcite grain boundaries. Grain boundaries were manually outlined as closed polygon using a vector-graphics application (Adobe Illustrator, v. 27.5), discarding those grains cut by the image margins. Combining the representative areas, over 1000 interconnected crystals per specimen were selected to ensure statistical reproducibility. Resulting maps were processed with ImageJ software (version 1.53t, by Wayne Rasband, https://imagej.nih.gov/ij/download.html) to get the calcite volumetric abundance, aspect ratio, and equivalent grain diameters. As second-phase minerals can affect the grain size (Ebert et al., 2008) e.g., placing themself as obstacles to grain boundary mobility (enhancing pressure solution mechanisms and/or grain boundary sliding) and/or growing competitively (Busch et al., 1995; Herwegh and Berger, 2004), we selected six specimens having the lowest percentage of second-phase minerals (35-20%, Table 2), showing no evidence of static recrystallization or later further microstructures affecting the grain size (see par. 4.1, 4.2). For each sample, the equivalent calcite grain size (expressed as the diameter of the equivalent circle, d) was calculated as the square root mean using GrainSizeTools v2.0.2 (Lopez-Sanchez and Funez, 2015). Paleopiezometric estimates were used to get the differential stress, σ, and the strain rate recorded by calcite deformed in the grain size insensitive (GSI) regime

(Renner et al., 2002, with references). The Barnhoorn et al. (2004) piezometer, designed for non-coaxial regime and calibrated for grain size data estimated through the linear intercept method, was adopted as $Log\sigma = (-0.82 \pm 0.15)\ log(d) + 2.73 \pm 0.11$.

As samples are affected by dynamic recrystallization, strain rate was calculated through the Renner et al. (2002) flow law, as $\dot{\varepsilon} = A\sigma^n \exp\frac{\sigma}{\sigma 0} \exp\left(-\frac{Q}{RT}\right)$, where A is the material constant (accounting for the chemical fugacity), n is the stress sensitivity (n=2), σ is the differential stress, σ_0 is the resistance to glide, Q is the apparent activation energy for the process, R the universal gas constant, and T is the deformation temperature.

Twin density (D) was also measured in appropriately oriented grains using ImageJ software on representative microphotographs (pixel resolution of 0.1 μm). Twins were analysed to estimate the differential stress using the Rybacki et al. (2011) piezometer. Since, to date, it is not clear how the critical resolved shear stress of twins varies with the grain size (e.g., Parlangeau et al., 2018), we selected a pool of crystals with homogeneous grain size. This choice does not affect the representativeness of the sample, as it can be inferred later from the study of the grain size (unimodal grain size, par. 4.2). Differential stress recorded by twinning was estimated through the equation $\sigma_{(twin)} = 10^{1.29\pm0.02}\ D^{0.5\pm0.05}$ (Rybacki et al., 2011). Strain rates from twinning mechanisms were calculated applying the exponential law by Rutter (1974) (see also Rowe and Rutter, 1990) as $Log\ \ \dot{\varepsilon}_{(twin)} = 5.8 - \left(\frac{250000}{2.303\mathrm{RT}}\right) + 0.038\ \sigma_{(twin)}$.

Finite-strain estimation with the centre-to-centre method (Fry, 1979) was performed on microphotographs from six rock specimens (Table 1) using calcite crystals as strain marker. About 100 to 225 crystals for each specimen were measured. Fabric ellipses, Rxz, were achieved applying the software EllipseFit 3.6.2 (by Frederick W. Vollmer, available at https://www.frederickvollmer.com/ellipsefit/). For an objective shaping of the ellipses, we used the exponential edge detection method (EED) of Waldron and Wallace (2007).

3.2. Analysis of Crystallographic Preferred Orientation (CPO)

Calcite and quartz crystallographic preferred orientations (CPOs) were investigated at the Geoscience Centre of the University of Göttingen on five and three specimens, respectively. Data were acquired with an X-ray Texture Goniometer (model X'Pert Pro MRD_DY2139 developed by PANalytical), specifically designed for rock samples with relative coarse grain sizes (Leiss and Ullemeyer, 2006) (Table 1). Measurements were made on rock's slides of c. 5 cm x 3.5 cm x 1-2 cm on the XZ planes (section parallel to the mineral lineation, normal to the foliation plane) with five to six spots for each slide, each spot of c. 7 mm of diameter. Additionally, measurements were performed on the YZ plane of the finite strain ellipsoid (section normal to the mineral lineation and macroscopic foliation) in those specimens where quartz CPO data were produced. Measuring CPOs on both planes allowed for a better pole figure coverage and, therefore, for a better estimation of the orientation distribution functions of the less abundant mineral phases (ODFs). To ensure the mineral phase composition at each slide, a 2Θ standard diffraction pattern of 5-75° has been measured.

Complete pole figures were recalculated from ODFs exploiting the MTEX Toolbox (MTEX 5.4.0, https://mtex-toolbox.github.io/) for Matlab of MathWorks (https://it.mathworks.com/products/matlab.html). For calcite cell parameters, we adopted a=b=4.988 Å, c=17.062 Å, and point group '312'; whereas for quartz we used a=b=4.913 Å, c=5.405 Å, and point group '312'. To reduce artefacts linked to data acquisition of larger crystals (that provide more intense peaks to the X-ray diffraction), the radially symmetric de la Vallee Poussin Kernel function (Schaeben, 1997) has been applied on ODFs calculation, with a halfwidth of 10° and a resolution of 5° (Hielscher and Schaeben, 2008).

3D patterns of the main crystallographic elements were plotted on equal area lower hemisphere stereographic projection (pole figures). Calcite and quartz CPO intensities were calculated from ODF applying the texture index (or J-index) of Bunge (1982), and the M-index of Skemer et al. (2005) as comparison.

3.3. Kinematic vorticity and shortening estimates

Estimating kinematic vorticity in naturally deformed rocks is often tricky as compositional and structural heterogeneities (typical in mylonite, e.g., SC-fabric, mica layering, etc.) are a prime cause of flow and strain partitioning (Handy, 1994; Jiang, 1994a, 1994b; Jiang and Williams, 1999; Kilian et al., 2011; Bhandari and Jiang, 2021). For this reason, we investigated the kinematic vorticity (sectional kinematic vorticity and mean kinematic vorticity, see Xypolias, 2010, for a review) and the resulting simple shear contribution only in the most homogeneous samples from representative areas of the detachment zone.

We applied two independents kinematic vorticity gauges on five suitable marble samples: the oblique foliation method (Wallis, 1995), and the calcite CPO orientation (Wenk et al., 1987; see Table 1 and Table 3). The sectional kinematic vorticity (Wn) was estimated by measuring the δ angle between the oblique foliation (Sb) and the mylonitic foliation (e.g., see Fig. 3). For each sample, the highest δ angle (consistent with the data distribution) was adopted (Wallis, 1995; Xypolias, 2010). From calcite CPOs, the simple shear contribution was achieved by measuring the ω angle between the main [c]-axes orientation and the plane normal to the mylonitic foliation (Wenk et al., 1987). In this case, the mean kinematic vorticity Wm (Passchier, 1997) can be derived from the obtained simple shear percentage assuming, for simplicity, a 2D flow (plane strain regime), in accordance with the flow regime recognized by Parsons et al. (2016b) in the close areas, and by Law et al. (2004) further to the east, in the Everest Massif.

The oblique foliation method allows us to estimate the vorticity of a small increment of ductile deformation linked to the onset of the development of the shape preferred orientation (Xypolias, 2010). Alternatively, the calcite CPO can record the simple shear contributions occurring during a large segment of the deformation history (Wenk et al., 1987).

4. Results

4.1. Microstructures and their interpretation

The study samples from the Annapurna Detachment zone consist of calc-silicate-rich marble and white marble belonging to the GHS_U, and biotite–muscovite metapsammite and marble of the Annapurna Fm.

from the THS (Fig. 2, Vannay and Hodges, 1996; Godin et al., 1999a). Interconnected calcite crystals are the 65-75% of the bulk volume in the GHS$_U$, and over the 65-80% in the Annapurna Fm. (Table 2; Fig. 3a-j), defining an interconnected weak matrix (Handy, 1994).

322

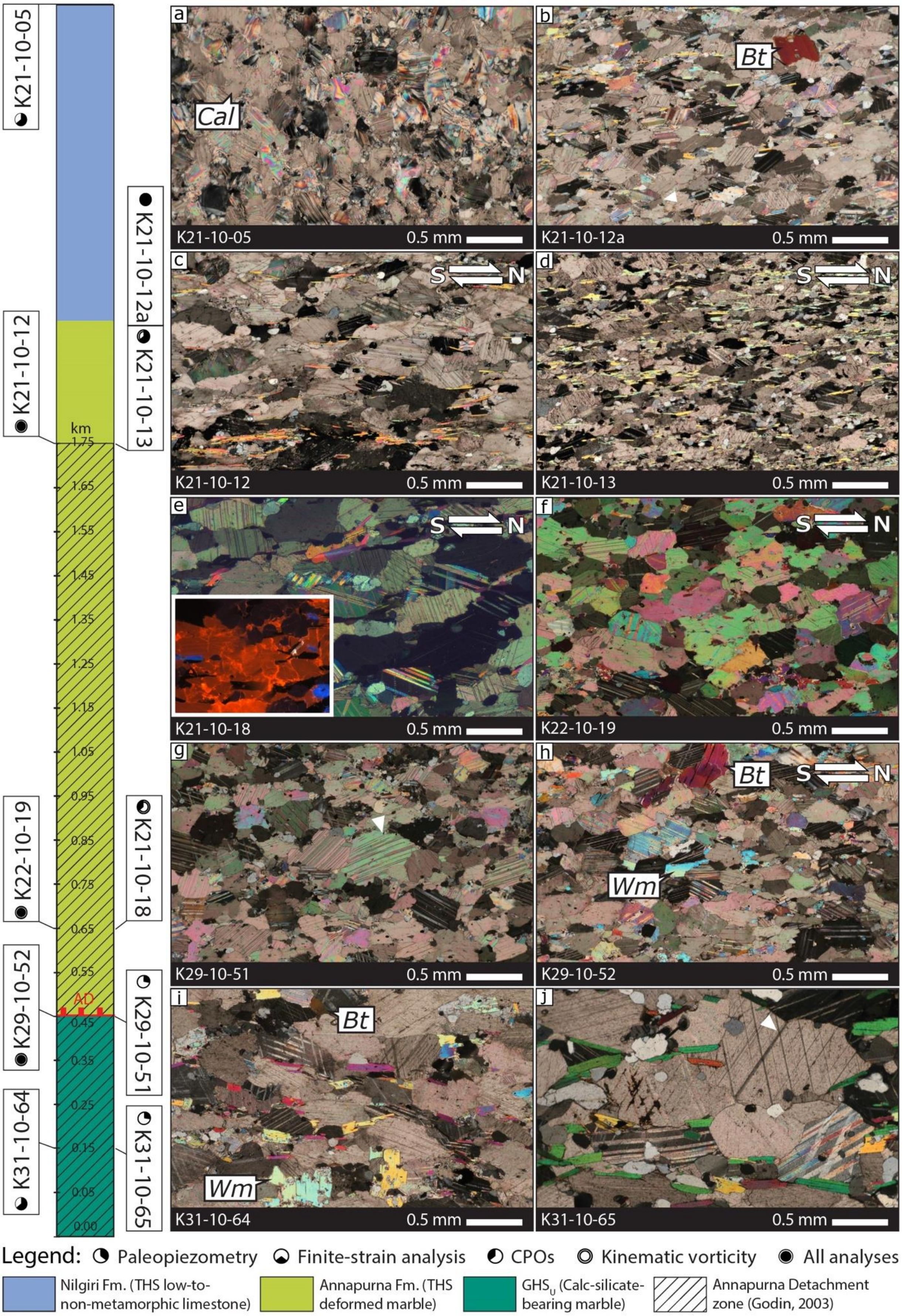

323 **Figure 3**

Biotite, muscovite, and calcite shape preferred orientation (SPO) defines the main continuous foliation (Sp). This fabric, correlated in literature to the mylonitic S2 foliation, develops from the GHS$_U$ to the Annapurna Fm. (THS) (see also Hodges et al., 1996; Vannay and Hodges, 1996; Godin et al., 1999a; Carosi et al., 2014; Parsons et al., 2016b, 2016c, 2016d). Calcite grains have an aspect ratio of c. 2–2.5 (Table 2) with a long axis ranging from parallel to high-angle with respect to the main foliation (Fig. 3c-f). In five samples (K21-10-12, K21-10-13, K21-10-18, K22-10-19, and K29-10-52) calcite oblique foliations (Sb) point toward the geographical north-direction. Calcite dynamic recrystallization is, therefore, syn-kinematic with the Annapurna Detachment top-to-the-north sense of shear (e.g., Fig. 3c-f).

At the bottom of the Annapurna Detachment zone, marbles belonging to the GHS$_U$ are coarse-grained (Fig. 3i-j). Straight grain boundaries, triple junctions, and a lack of undulous extinction in the lowermost sample (K31-10-65, Fig. 3j) are interpreted as indicative of static recrystallization or post-kinematic growth (e.g., Molli et al., 2000; Ohl et al., 2021), as also suggested by Brown and Nazarchuk (1993) and Vannay and Hodges (1996). Large white micas and biotite crystals, often overprinting the S2 foliation, show poikilitic structures (e.g., Fig. 3b, h, i), indicating a local post-mylonitic static recrystallization in the GHS$_U$.

In the THS, within the Annapurna Fm. (e.g., K21-10-18; K22-10-19 at the base, K21-10-12, K21-10-13 above, Fig. 3b-f) calcite lobate grain boundaries and undulous extinction are typical microstructures for intracrystalline deformation and dynamic recrystallization (Molli and Heilbronner, 1999; Molli et al., 2000; Barnhoorn et al., 2004). Calcite grain size distribution in these samples is unimodal (Fig. 4), whereas at the top (e.g., K21-10-12a) it becomes slightly bimodal, with rare calcite ribbons and porphyroclasts. Unimodal grain size, lobate grain boundaries and little undulous extinction in calcite in marbles at the base can be interpreted as resulting from the superimposition of grain boundary migration (GBM) recrystallization regime on subgrain rotation recrystallization (SGR) regime (e.g., Busch et al., 1995; Molli et al., 2000; Piazolo and Passchier, 2002; Stipp et al., 2002; Ulrich et al., 2002; Rogowitz et al., 2014, 2016). Type II and Type I twins overprint most calcite host grains (Fig. 3, Fig. 5a). Thin twins often develop parallel to thicker tapered twins (Fig. 3g, 4b).

Only in few specimens, close to the GHS_U, intercrystalline fractures, calcite veins and fluid inclusions trails at a high angle to the main foliation point out partly healed post-mylonitic brittle deformation, without affecting the recognizability of the original grain size, developed by dynamic recrystallization. Hot-cathodoluminescence images reveal evidence of minor overgrowths on calcite and thin recrystallized (bright red) rims indicating Mn^{2+} rich fluids recrystallization in calcite (Boggs and Krinsley, 2006) e.g., in sample K21-10-18, where calcite shows straight grain boundaries (see Fig. 3e). Micas (non-luminescent phases in Fig. 3e) are undeformed and often interstitial between the calcite rims in such specimens. Such features should be likely due to a fluid circulation linked to the Dhumpu Detachment late reactivation (Pye et al., 2022).

Within small asymmetric lens-shaped quartz aggregates, crystals are incipiently deformed (e.g., samples K21-10-12a, THS, and K21-10-18, at the boundary with GHS_U). Out of the aggregates (e.g., Fig. 3c, j), quartz occurs as rounded strong clasts within the weak calcite matrix.

4.2. Paleostress and paleotemperature estimations

To avoid overestimation of the grain size due to the (local) annealing, six representative purer specimens with no evidence of static recrystallization have been selected. This choice does not affect the representativeness of the grain size results, as static recrystallization does not seem to have particularly affected the grain size of the annealed samples (e.g., Fig.2e, par. 4.1). Calcite mean grain size in samples deformed by GBM varies from bottom to top (Fig. 4), with equivalent diameters from 770 μm, in the GHS_U, to 390 μm in the Annapurna Fm. Recrystallized grains in sample at the top (K21-10-12a), deformed by SGR, have a mean grain size of 250±30 μm (Table 2). Applying Barnhoorn et al. (2004) piezometer for these samples, differential stress values are in the range of 4-19 MPa (Table 2). The Renner et al. (2002) relation for strain rates was applied once deformation temperatures were inferred (Table 2). For the GHS_U marbles (K29-10-51, K29-10-52, K31-10-64), a deformation temperature of c. 500°C (773.15 K) was adopted, as it is in the range proposed by Parson et al. (2016b) through quartz and dolomite microstructures for the basal part of the ductile detachment in the Kali Gandaki and Modi Khola valleys (300-600°C, Parson et al., 2016b, and up to 700°C probably during the previous stages, see Parsons et al., 2016d) and, for similar structural levels, by Schneider and Marsh (1993) based on the metamorphic assemblage and petrological insight (500-530°C for the GHS_U involved by the Chame Detachment, the prosecution of the STDS in the Marsyandi valley).

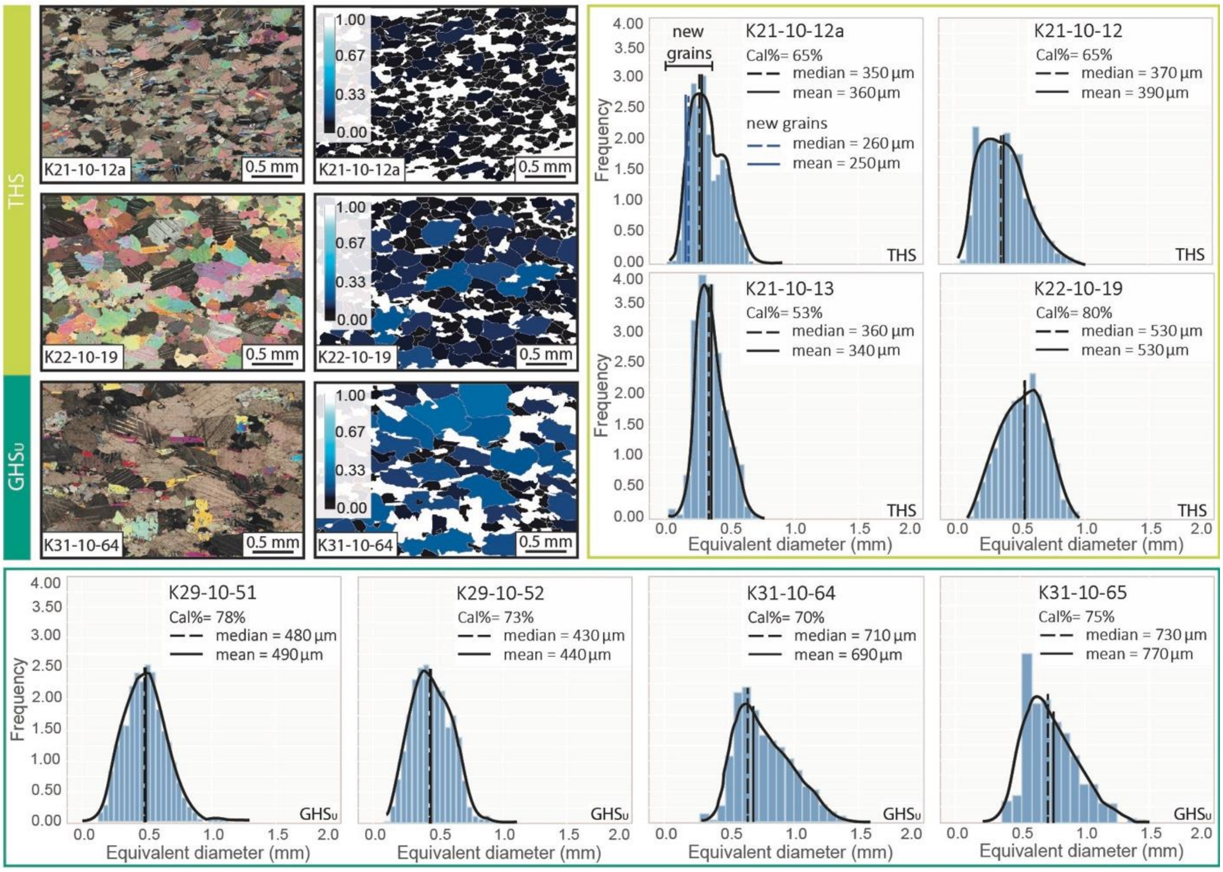

Figure 4

A deformation temperature average of c. 400°C (673.15 K) was adopted for THS rocks (samples K21-10-12, K21-10-12a, K22-10-19) following the main estimations for similar structural levels, close to the study area (300-500°C, Parsons et al., 2016b), and in the nearby Marsyandi valley (440-370°C, Schneider and Marsh, 1993). The corresponding strain rates for these deformation temperatures are of 8.1×10^{-10}-1.3×10^{-9} s^{-1} in the GHS_U, and of 1.1×10^{-11}-3.1×10^{-11} s^{-1} in the THS marbles (Table 2).

Type II *e*-twins have a thickness of c. 3-4 µm and a mean twin density of c. 40-55 (normalized to 1 mm length) (Fig. 5a, b; Table 2). According to Ferrill et al. (2004), the comparison of the mean twin width and the mean twin density is correlated to the deformation temperature. In our specimens, this ratio implies that the main twins' development occurred at temperatures below 300°C, likely of c. 200-250°C

(Fig. 5c). Crystals with thicker and spaced tapered twins, on which finer twins are superimposed, may indicate a progressive decrease in temperature from T>250°C to T<200°C (Ferrill et al., 1998, 2004).

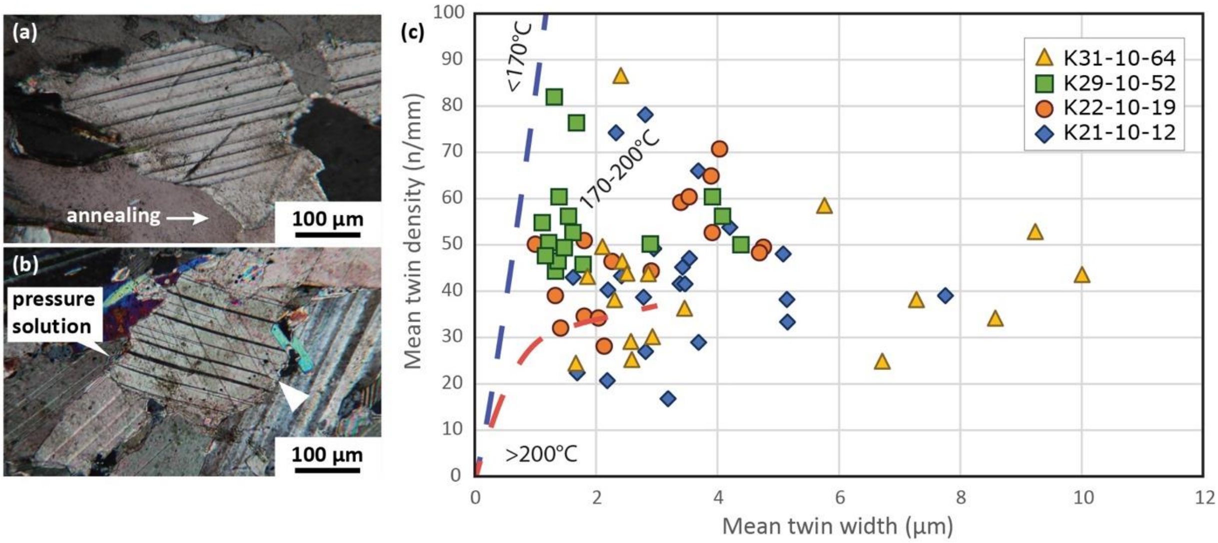

Figure 5

According to Rybacki et al. (2011) piezometer, twin density developed for differential stress of 118-154 MPa (Table 2). As *e*-twins typically dominate on the other deformation mechanisms at T<400°C (Groshong, 1988; Burkhard, 1993), and the mean twin width *vs* the mean twin density ratio indicates deformation temperatures down to 200-250°C (Ferrill et al., 2004), we adopted an average temperature of 250°C (523.15 K) for estimating strain rates linked to the shifting from dynamic recrystallization to twinning as dominant deformation mechanism accounting that the twins induced by the non-coaxial deformation continued to be generated at the lower temperatures proposed by the graph. The resulting strain rates are in the range of 4.4 x 10^{-15} - 2.2 x 10^{-14} s^{-1} (Table 2).

4.3. Crystallographic preferred orientation (CPO) data and interpretation

Quartz, occurring in small asymmetric lenses or as isolated stronger clast within calcite matrix (two samples belonging to the THS, one from the GHS_U), have been analysed for the CPOs. Quartz has weak CPOs intensity, defined by J-index of 1.16 and M-indexes of 0.01 (almost close to a total random distribution, see Skemer et al., 2005), with multiples of uniform distribution in the range 0.7–2.2 (expressed as min-max in Fig. 6a-c). From bottom to top, the [*c*]-axes on [0001] pole figures define clockwise asymmetric single girdle distributions suggesting dextral non-coaxial shear (Fig. 6a, Lister, 1977; Schmid and Casey, 1986). Couples of maxima are close to the Y-direction of the finite strain ellipsoid (Fig. 6a-c).

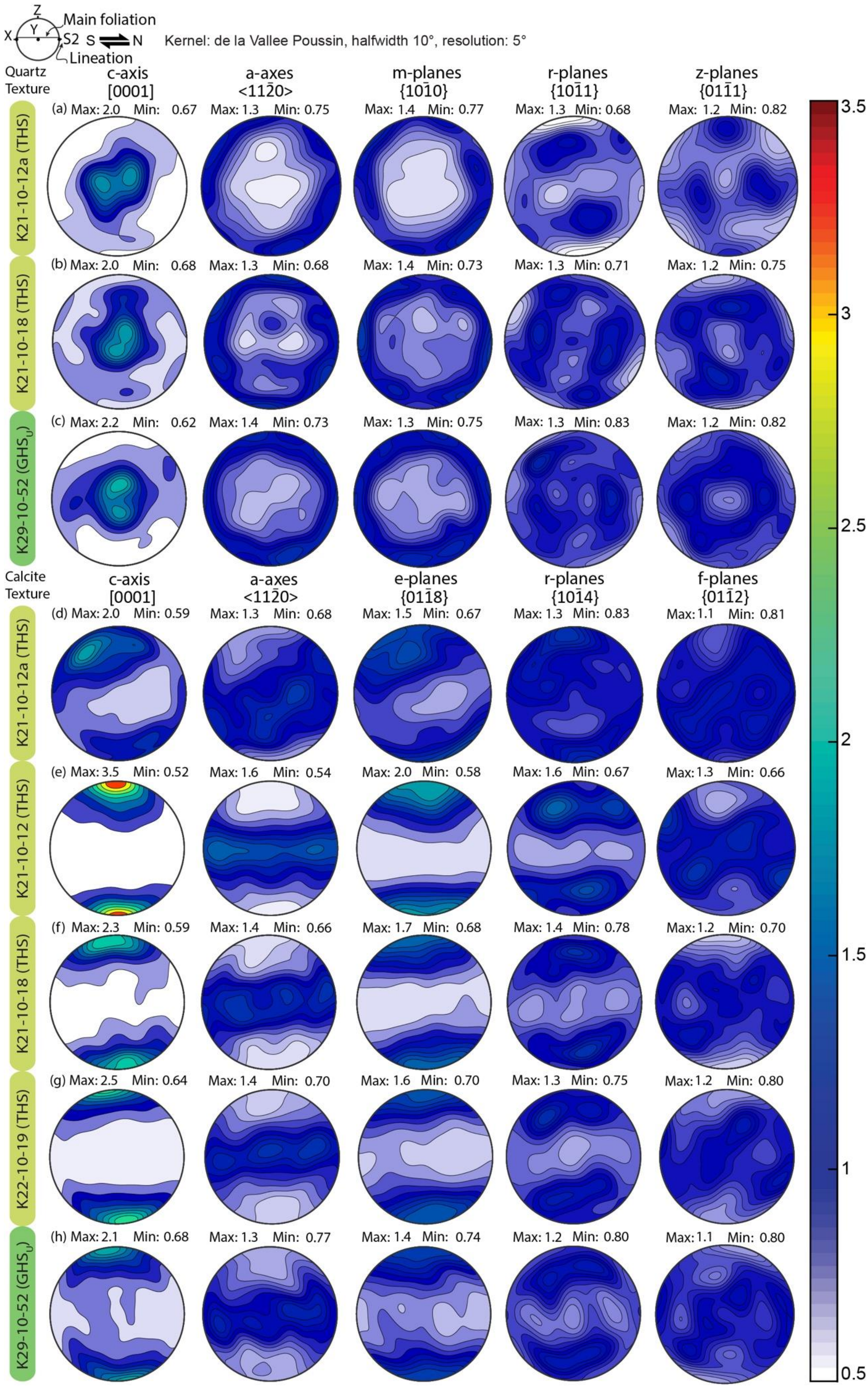
Main foliation
X
Y
Z
S2 S N
Lineation
Kernel: de la Vallee Poussin, halfwidth 10°, resolution: 5°
Quartz Texture
c-axis [0001]
a-axes <11$\bar{2}$0>
m-planes {10$\bar{1}$0}
r-planes {10$\bar{1}$1}
z-planes {01$\bar{1}$1}
(a) Max: 2.0 Min: 0.67 Max: 1.3 Min: 0.75 Max: 1.4 Min: 0.77 Max: 1.3 Min: 0.68 Max: 1.2 Min: 0.82
K21-10-12a (THS)
(b) Max: 2.0 Min: 0.68 Max: 1.3 Min: 0.68 Max: 1.4 Min: 0.73 Max: 1.3 Min: 0.71 Max: 1.2 Min: 0.75
K21-10-18 (THS)
(c) Max: 2.2 Min: 0.62 Max: 1.4 Min: 0.73 Max: 1.3 Min: 0.75 Max: 1.3 Min: 0.83 Max: 1.2 Min: 0.82
K29-10-52 (GHS_U)
Calcite Texture
c-axis [0001]
a-axes <11$\bar{2}$0>
e-planes {01$\bar{1}$8}
r-planes {10$\bar{1}$4}
f-planes {01$\bar{1}$2}
(d) Max: 2.0 Min: 0.59 Max: 1.3 Min: 0.68 Max: 1.5 Min: 0.67 Max: 1.3 Min: 0.83 Max: 1.1 Min: 0.81
K21-10-12a (THS)
(e) Max: 3.5 Min: 0.52 Max: 1.6 Min: 0.54 Max: 2.0 Min: 0.58 Max: 1.6 Min: 0.67 Max: 1.3 Min: 0.66
K21-10-12 (THS)
(f) Max: 2.3 Min: 0.59 Max: 1.4 Min: 0.66 Max: 1.7 Min: 0.68 Max: 1.4 Min: 0.78 Max: 1.2 Min: 0.70
K21-10-18 (THS)
(g) Max: 2.5 Min: 0.64 Max: 1.4 Min: 0.70 Max: 1.6 Min: 0.70 Max: 1.3 Min: 0.75 Max: 1.2 Min: 0.80
K22-10-19 (THS)
(h) Max: 2.1 Min: 0.68 Max: 1.3 Min: 0.77 Max: 1.4 Min: 0.74 Max: 1.2 Min: 0.80 Max: 1.1 Min: 0.80
K29-10-52 (GHS_U)
3.5
3
2.5
2
1.5
1
0.5

Figure 6

We interpret that the wide girdle distribution resulted by a mix of rhomb<*a*> and prism<*a*> ± basal/π'<*a*> slip (e.g., Toy et al., 2008; Morales et al., 2011, 2014, with references), with further mechanical grains rotation attenuating the CPO intensity (Stallard and Shelley, 1995). Alternatively, we propose that the broad peripheral [*c*]-axis distribution derive from a large contribution of dislocation-induced grain boundary sliding and subordinate dislocation glide (Kilian and Heilbronner, 2017), determining the weak CPO strength (Graziani et al., 2020). In both cases, we interpret quartz CPOs as due to intracrystalline deformation under a non-coaxial flow. Comparing the asymmetry of the fabric (with respect to the orientation of the foliation and the lineation) with the original geographic orientation, the dextral non-coaxial shear is consistent with the top-to-the-north ductile shearing of the Annapurna Detachment zone (Fig. 6a-c).

Calcite CPOs strength, defined by the J-index of 1.09-1.39 and the corresponding M-index of 0.02-0.04, is quite constant between samples, with multiples of uniform distribution in the range 0.5-3.5 (Fig. 6d-h). The clear calcite CPO patterns support that calcite grains have been strongly reoriented during deformation despite of structural anisotropies and/or to the second-phase mineral amount/distribution (Olgaard, 1990; Hippertt, 1994; Tullis and Wenk, 1994; Herwegh and Berger, 2004; Graziani et al., 2020). Broad [*c*]-axis point maxima are close to the Z-axis of the finite strain (almost normal to the foliation), while <*a*>-axes form girdles sub-parallel to the XY plane (Fig. 6d-h). In the uppermost sample, K21-10-12a, where the [*c*]-axis point maxima are strongly inclined, the poles to the rhombic planes $\{10\bar{1}4\}$ are weakly focussed on point maxima normal to the foliation plane, while poles to the {*e*}-planes (on $\{01\bar{1}8\}$ pole figure) define couples of strong asymmetric maxima inclined toward the left (Fig. 6d). In all other analysed samples, the poles to the rhombic planes $\{10\bar{1}4\}$ and $\{01\bar{1}2\}$ define weak small circles distributions (Fig. 6e-h). Point maxima of the {*e*}-planes poles are inclined toward the left with respect to the foliation pole (Fig. 6e-h). For all specimens, a top-left asymmetry (Fig. 6d-h) is antithetic to the calcite oblique foliations orientations measured on the same XZ-plane (Fig. 3c-f, h), and to the quartz CPOs asymmetry (Fig. 6a-c).

The interpretation of calcite CPOs in terms of slip systems is not straightforward (Ohl et al., 2021, with references). In all study samples, calcite CPOs can be due to the high-temperature basal<*a*> slip (during grain boundary migration mechanisms) or to the coupled activity of rhomb<*a*> slip and *e*-twinning, or to both (HT basal<*a*> slip followed by LT rhomb<*a*> slip and *e*-twinning). In the sample at the top (K21-10-12a), the peripheral asymmetric couples of maxima for the [*c*]-axis, the {*e*}-planes and the {*r*}-planes let us lean towards the coupled activity of rhomb<*a*> slip and *e*-twinning. Indeed, *e*-twinning can strongly rotate calcite [*c*]-axes against the sense of shear (Wenk et al., 1987; Lacombe, 2010; Tripathy and Saha, 2015), also favouring the slip along the {*r*}-planes (Oesterling et al., 2007). Concerning the other samples, the observed CPO can be potentially related to the activity of any calcite slip system. However, the strong maxima of the [*c*]-axes and the {*e*}-planes, and the absence of peripheral maxima in the pole figures of the {*r*}- and {*f*}-planes, are consistent with a CPO balanced by *e*-twinning or basal<*a*> slip alone. Different degrees of [*c*]-axis maxima inclination in most samples point out heterogeneous deformation (Kern and Wenk, 1983; Wenk et al., 1987), while the symmetry of the [*c*]- and {*e*}-maxima in sample K21-10-12 (Fig. 6e, about 2° of asymmetry to the left) indicates a CPO equilibration under dominant pure shear conditions (Wenk et al., 1987). In general, calcite CPOs top-to-left asymmetry is consistent with an antithetic orientation linked to intracrystalline deformation accommodated under a top-to-right non-coaxial flow. The top-to-right non-coaxial flow observable on the XZ-plane of the finite strain is geographically consistent with the top-to-the-north sense of shear of the Annapurna Detachment zone.

4.4. Kinematic vorticity and shortening of the flow: results and interpretations

The Wenk et al. (1987) method (Fig. 7a, Table 3) provided the simple shear contribution in four samples (K21-10-12, K21-10-18, K22-10-19, K29-10-52). We discarded specimen K21-10-12a as the [*c*]-axis maxima do not fall on the primitive circle (Fig. 6d) and its CPO is, therefore, over inclined for the Wenk et al. (1987) method. *Vice versa*, we kept in the sample the specimen K21-10-18 (despite we previously interpreted as affected by little static recrystallization) since the superimposition of incipient annealing should not have affected the orientation of the fabric but its intensity (Barnhoorn et al., 2005; Herwegh et al., 2008), and it does not seem affected by the late brittle deformation associated to the Dhumpu Detachment defined by Pye et al. (2022). Among the sample, the ω° angle between the [*c*]-axis maxima and the pole to the mylonitic foliation indicates a contribution from c. 30% to c. 50% of simple shear for specimens K22-10-19, K29-10-52, and K21-10-18 (Fig. 7a, Table 3). A lower simple shear is deduced for the specimen K21-10-12, where almost symmetric [*c*]-axis maxima are displayed (Fig. 6e). Assuming a plane strain deformation, as inferred through quartz CPO studies on the regional structure of the STDS from Eastern Nepal to Western Nepal (e.g., Law et al., 2004, 2011; Parsons et al., 2016b), the percentages of simple shear of specimens K22-10-19, K29-10-52, and K21-10-18 correspond to a mean kinematic vorticity (Wm) of 0.45-0.71 (Table 3, Fig. 7b).

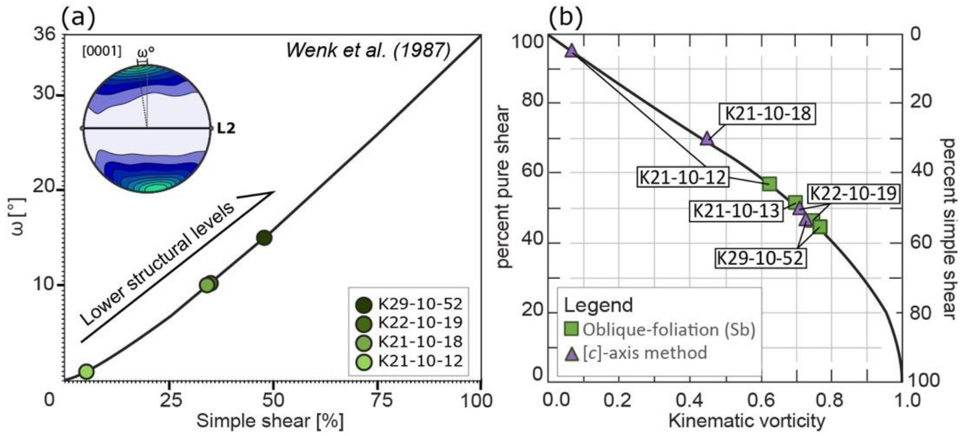

Figure 7

The Wallis (1995) method for the sectional kinematic vorticity (Wn) was applied on four samples (K21-10-12, K21-10-13, K22-10-19, and K29-10-52, Table 3) where oblique foliations (Sb) are more evident and statistically developed (e.g., Fig. 3c-f). The δ° angles between the Sb and the main foliation decrease up-section from c. 26 to 20°, corresponding to Wn=0.79-0.64 (Table 3). For the same assumptions used for the previous method (i.e., plane strain deformation), the sectional kinematic vorticity range indicates a contribution of c. 40-50% of simple shear (Table 3, Fig. 7b).

With the exclusion of the uppermost samples (K21-10-12), we observe that both oblique foliation and twinning-influencing calcite CPOs recorded comparable and quite consistent subsimple shear flow conditions (Fig. 7b) even considering intrinsic limitations of vorticity gauges (e.g., the assumption of a nearly plane strain dominated deformation, Iacopini et al., 2008; Xypolias, 2010; Fossen and Cavalcante, 2017).

In general shear, the coaxial component of the deformation is connected to the shortening perpendicular to the flow plane (layer parallel extension) as a function of the finite strain (Wallis et al., 1993). The finite-strain equivalent ellipse ratios (R_{XZ}) of six specimens (K21-10-12a, K21-10-12, K22-10-19, K29-10-52, K31-10-64, and K31-10-65; Table 1) range between 1.24 to 1.58, and slightly increase down-section within the Annapurna Detachment zone vertical profile (Fig. 8, Table 3). Shortening values of 0.89-0.92 and of 0.86-0.87 (Table 3) are then obtained combining the finite-strain ratio (R_{XZ}) with the kinematic vorticity estimates after Wallis (1995) method and the Wenk et al. (1987) method, respectively.

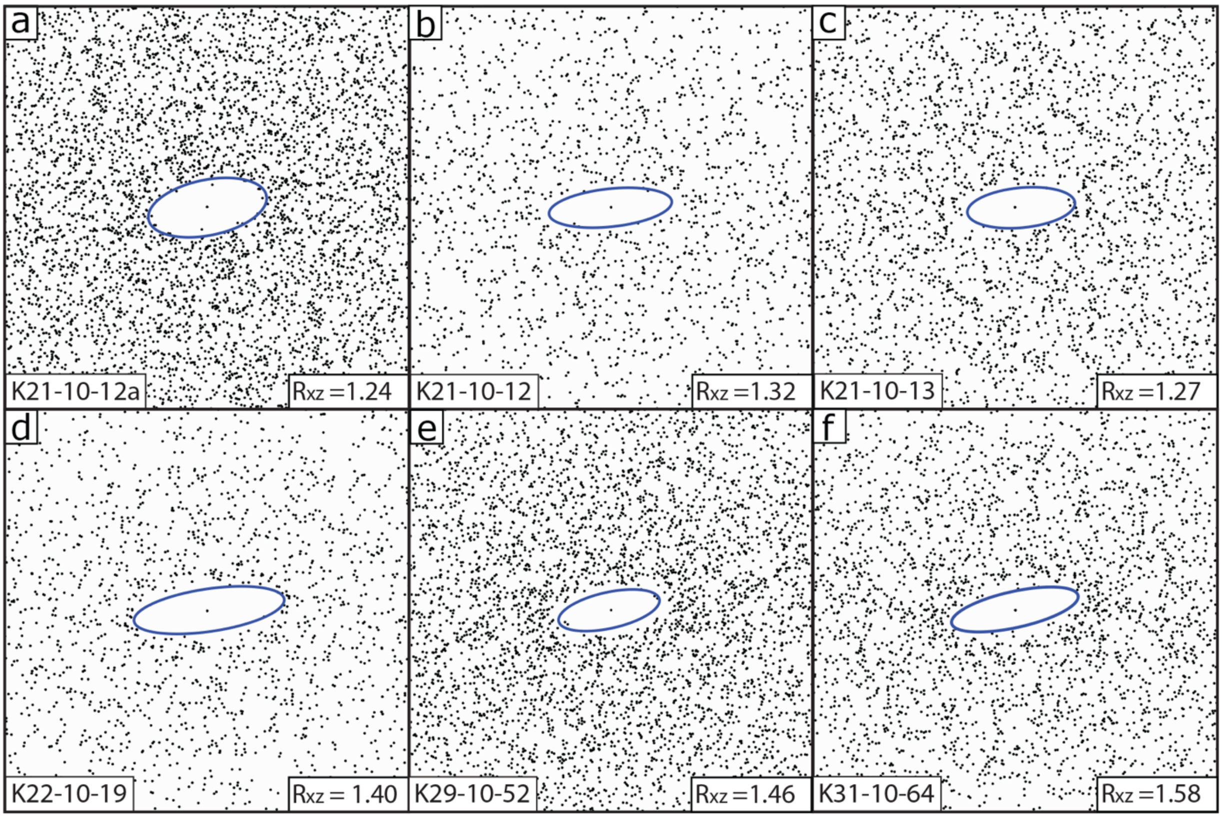

Figure 8

5. Discussion

5.1. Deformation style of the Annapurna Detachment zone

A concept typically adopted for studying shear zones is “self-similarity”, i.e., the attitude of rocks to produce consistent structures from the large scale to the microscale. In marble mylonites of the Annapurna Detachment zone, calcite grains define the weak interconnected matrix, accounting over

65% of the bulk volume in each specimen (*Table 2*). Calcite constitutes the main weak phase accommodating the overall deformation (e.g., Handy, 1994) and, as this trait occurs in the whole sampling, we can scale up the picture we have from the microanalysis to infer large-scale information for the detachment zone. Moreover, marble mylonites involved by the Annapurna Detachment zone show remarkable lithological affinities with the nearby STDS in the Dolpo region to the west (Fig. 1, see Carosi et al., 2002, 2007) and in the Modi Khola and Marsyandi valleys (close to the Manaslu range in Fig. 1) to the east (Schneider and Masch, 1993; Searle, 2010; Parsons et al., 2016b, 2016d; Carosi et al., 2023). This allows us to exploit the literature database for detachment as external constraints to add to our microstructural investigation.

Calcite and quartz fabric and CPOs have clear patterns related to a plastic deformation, like those identified in the area by Parsons et al. (2016b). Microstructural and calcite CPOs data allowed us to recognize two dominant deformation mechanisms that we can use to picture the main deformation parameters: (1) dynamic recrystallization by GBM/SGR, determining the grain size distributions and the oblique foliations; (2) type II twinning of calcite crystals. From our analyses of the kinematic indicators at the microscale (e.g., Fig. 3c-f, h), and by pole figures data interpretation (Fig. 6), both intracrystalline processes accommodated a ductile deformation under a top-to-the-north non-coaxial flow (Fig. 7b) consistent with the Annapurna Detachment zone shearing. Kinematic vorticity estimates based on the oblique foliation method (related to dynamic recrystallization) and the CPO (balanced by twinning) are consistent with only one outlier (Fig. 7b) for a sample at the detachment external limit (Fig. 2). A main 40-50% of simple shear is constrained for Wn=0.64-0.79 through the oblique foliations (Wallis, 1995), that is consistent with the simple shear range of 30-50% derived from calcite CPOs (Wenk et al., 1987; Fig. 7b). The presented data are a semi-quantitative result because the reference frame adopted is the mylonitic foliation instead of the exact shear plane. In natural shear zones, it is recurrently assumed that the mylonitic foliation is in close parallelism with the shear plane. In our case, this assumption does not compromise the result as our samples belong to a high strain zone, where the pervasive mylonitic foliation accommodated a huge amount of strain (Godin et al., 1999a). A detachment-parallel transport magnitude of 25-170 km has been estimated e.g., by Law et al. (2011) for the regional prosecution of the detachment system in the Everest area, confirmed toward the east by Long et al. (2019) in NW Bhutan. This extreme magnitude of tectonic transport allows to assume that the mylonitic foliation had neglectable variations in angle with the shear plane from a regional perspective (Fossen, 2016). Moreover, the kinematic vorticity estimates that we propose for the Annapurna Detachment zone (0.64-0.79) fit with the one estimated for the STDS in the Everest area, where kinematic vorticity data of 0.67-0.98 are reported by Law et al. (2004and Larson et al. (2020) through the porphyroclasts-based (Wallis et al., 1993; Simpson and De Paor, 1997) and the quartz [*c*]-axis based (Wallis, 1992) vorticity gauges. Similar kinematic vorticity values (Wm = 0.74–0.91), supportive for a simple shear dominated flow with a critical component of pure shear, have been found also in the sheared limestone and marble of the THS by Jessup et al. (2006) in the same area. The minor differences between our estimates (up-to Wm=0.79) and previous proposed kinematic vorticity data possibly depend on the strain partitioning of the complex heterogeneous STDS from area to area. This can be due to the different involved lithologies and the different strain memory of the analysed structures.

The centrepiece of comparing the two kinematic vorticity gauges adopted methods (oblique foliation and CPOs) is that the same reference frame has been used. Therefore, regardless of how quantitative the result may be, our data indicate that both structures, deriving from the two intracrystalline deformation mechanisms, developed not only for the same kinematics but with comparable simple shear contribution during the non-coaxial flow.

5.1.1. Evolution of the deformation of the marble mylonite of the Annapurna Detachment zone

To unravel whether dynamic recrystallization and twinning reflect a single step of the long-lasting shearing (active together) or a progressive change in the plastic regime during the exhumation/cooling path (an early and a late stage of shearing), hereafter we focus on the differential stress, the deformation temperature, and the strain rate estimates. We will later compare these results with the literature database for the Nepalese areas to visualize the differences and similarities of the detachment system when involving marbles instead of quartz-bearing lithologies. There are several works showing that grain boundary mobility and twinning can develop together for the same deformation conditions, at

T<400°C, and for low differential stress (e.g., Schmid et al., 1987; De Bresser and Spiers, 1993; 1997). Twinning produces high-angle boundaries, in which reticular defects and the stored elastic energy accumulate, triggering twin/grain boundary mobility mechanisms at MT-HT conditions, or pressure solution/solution transfer at LT conditions (Lafrance et al., 1994). The main tool to verify in which regime the deformation has been accommodated is the comparison of the differential stress and deformation temperature.

Our data indicates that the differential stress, the deformation temperature, and the strain rate estimable for GBM/SGR and twinning are different (Table 2). We propose differential stress values of 4-19 MPa for the grain size development (adopting Barnhoorn et al., 2004, paleopiezometer) and of 118-154 MPa for twinning (after Rybacki et al., 2011 paleopiezometer; Table 2). For the dynamic recrystallization mechanism, equivalent results have been reported for the Everest area (Law et al., 2011; Waters et al., 2019). Adopting the Stipp and Tullis (2003) quartz-based piezometer, Law et al. (2011) and Waters et al. (2019) provided differential stress records of 10–15 MPa at the base of the STDS, and strain rates of 10^{-12}-$10^{-15}s^{-1}$ from the base of the detachment to almost 600 m of vertical distance. Concerning the twin density paleopiezometer, differential stress values as those estimated in this work for twinning in calcite (>100 MPa) are not excessively high when compared with data from other Low-Angle Normal Faults (e.g., the Whipple detachment in South-eastern California, Axen, 2004, 2019) and are consistent with results obtained in the Lower Dolpo region for the same structure in the STDS marbles (Nania et al., 2022b). Nevertheless, the inferred differential stress to produce twins in calcite is about one order of magnitude higher than that required for dynamic recrystallization.

The comparison between the deformation temperatures for the two intracrystalline mechanisms is more complicated and requires an interdisciplinary approach. During shearing at mid- to upper-crustal levels, slow grain boundary migration in calcite controls grain boundary morphology for a wide temperature range (Lafrance et al., 1994) and different nature of intercrystalline fluid (Schenk et al., 2005). Furthermore, equivalent CPOs can form at temperatures above 500°C down to T<150°C (e.g., Molli et al., 2010; Verberne et al., 2013; Bauer et al., 2018; Sly et al., 2020, with references; Lacombe et al., 2021). There are currently no calibrations for calcite slip system activation as geothermometer that consider the role of fluids and the abundance and composition of second-phase minerals (e.g., Ohl et al., 2021). For this reason, calcite features must be compared with those of the metamorphic minerals that are typically indicators of the deformation temperature. Calcite shape preferred orientation (SPO) is consistent with that of calc-silicates and main metamorphic minerals (Fig. 3). This indicates that calcite recrystallization is syn-tectonic with the metamorphic assemblage indicative of the metamorphic facies. Amphibolite facies assemblage of GHS_U prosecutes throughout the Annapurna Fm. base (THS), decreasing abruptly to greenschist facies in few hundreds of meters (see also Garzanti and Pagni Frette, 1991; Garzanti et al., 1994; Hodges et al., 1996; Vannay and Hodges, 1996, Crouzet et al., 2007; Parsons et al., 2016b). These two metamorphic facies let us consider a main temperature range of 500-600°C for the GHS_U, and of at least 400°C for the base of the THS that is involved by the detachment zone. This temperature range is consistent with the one proposed in close areas e.g., by Parsons et al. (2016b) for two transects in the Kali Gandaki and Modi Khola valleys through quartz and dolomite microstructures, especially when compared with the deformation temperature associated to the GHS_U. It is also consistent with the petrological constraints (i.e., calcite/dolomite geothermometer) of Schneider and Masch (1993) and of Crouzet et al. (2007) in close areas, where the temperature proposed from the top of the GHS_U to the biotite-zone of the THS are of 520-390°C. Similar estimates for the GHS_U (c. 500°C) have been proposed through the analysis of quartz microstructures combined with petrological constrains by Nagy et al. (2015) and Soucy La Roche et al. (2018) for the upper Karnali valley of Western Nepal (520°C for structural levels comparable with those of our samples) and in the Everest area in Eastern Nepal (Law et al., 2004, 2011; Cottle et al., 2011; and Waters et al., 2019). Such data rely on different geothermometers, such as quartz CPO and opening-angle thermometry (Law et al., 2004, 2011), Raman spectroscopy on carbonaceous material (Cottle et al., 2011), and petrological constraints (Waters et al., 2019). Especially with reference to Law et al. (2011), we highlight that the range of deformation temperatures for the rocks at the base of the detachment (GHS_U) has been precisely associated with the mechanisms of dynamic recrystallization and the oblique foliation, as in our case for the syn-kinematic recrystallization of calcite. Therefore, we hypothesize that the part of the detachment shearing accommodated by dynamic recrystallization and oblique foliation development occurred at mid-temperatures conditions of 500/550-400°C (from the base to the top of the involved volume).

By contrast, our temperature estimates for twins are significantly lower (Fig. 5c). According to the semi-quantitative thermometer, e-twins developed down to (at least) 250°C and, in any case, twinning starts to be a dominant mechanism able to re-orient the CPOs at deformation temperatures below 400°C (Groshong, 1988; Burkhard, 1993). Therefore, not only the differential stress values but also the deformation temperatures associated with the dynamic recrystallization and twinning are significantly different.

For the temperature and the differential stress ranges that we obtained, the strain rate required for dynamic recrystallization of calcite (c. 10^{-11} s^{-1}) is greater than the results for twinning development (of. C. 10^{-15}-10^{-14} s^{-1}) (Table 2). The methods used to calculate strain rates for GBM (Renner et al., 2002) are probably not effective for acquiring quantitative estimates of impure marbles. Overall, unlike the case of twinning, for little temperature variations in the calculation of the strain rates for GBM, the resulting values change by several orders of magnitude. All of it make us suspicious that our estimates for the strain rate of calcite recrystallization are underestimated. However, even without considering the results for the strain rate for GBM quantitatively, we suggest that for higher temperatures and lower differential stresses the strain rate required for plastic deformation must be faster than that necessary for the combination of lower temperature and higher differential stress, necessary for twinning. Therefore, we propose that marbles recorded a (not yet quantifiable) slowing of the deformation during the Annapurna Detachment zone ductile shearing, in addition to the lowering in deformation temperature and the increase of differential stress.

For a normal continental geothermal gradient of 25–40°C/km, in accordance with the typical lithospheric strength profiles, a differential stress of ≤15 MPa at temperatures of 400-500°C (recorded by the syn-kinematic dynamic recrystallization) occurs in the middle-upper crust under ductile deformation conditions. *Vice versa*, a high differential stress at low temperature conditions for viscous-like deformation (recorded by twins) usually occurs in the brittle-ductile transition (Fig. 9). Combining all the microstructural data with, CPOs, metamorphic facies, and temperatures from the literature database, we propose that the two deformation mechanisms reflect two stages of progressive ductile shearing of the Annapurna Detachment zone in the Kali Gandaki valley (Fig. 9):

- D2$_{early}$, recorded by calcite (and quartz) intracrystalline deformation, and characterized by a down-section lowering of differential stress (range of 4-19 MPa) and increase of deformation temperature (from 400°C in the THS to at least 500°C in the GHS$_U$) within the vertical Annapurna Detachment profile, under "fast" strain rates.
- D2$_{late}$, recorded by twinning in calcite, defined by high differential stress (118-154 MPa) and low deformation temperatures (down to 250°C), under lower strain rates (of c. 10^{-14} s^{-1}).

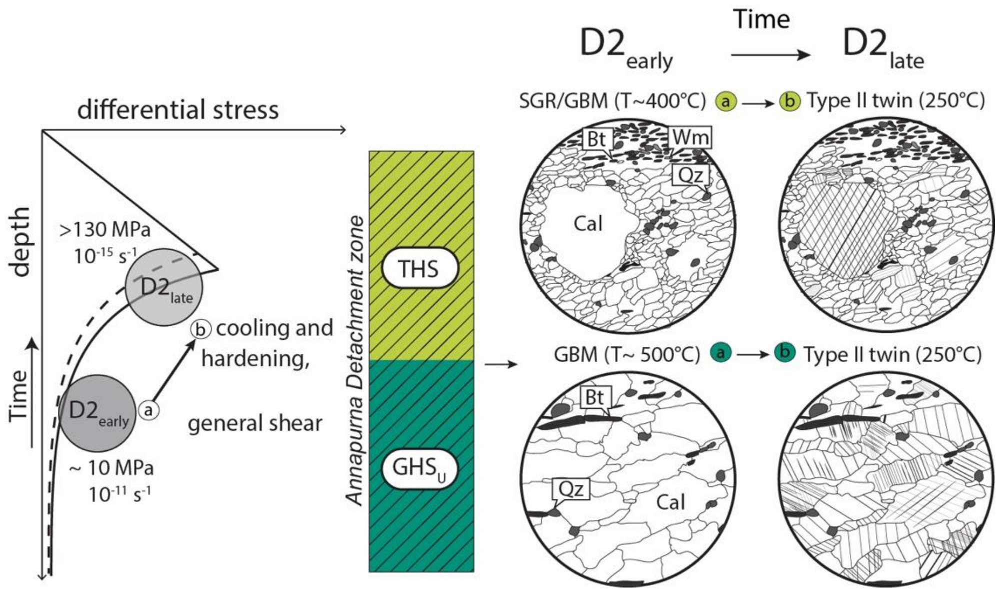

Figure 9

We therefore suggest that both dynamic recrystallization and twinning are not simply linked to multiple activation pulses of the ductile Annapurna Detachment zone. The ductile flow within the Annapurna Detachment zone protracted up to shallow crustal levels, close to the epizone/anchizone. After the cessation of the plastic shearing, at temperatures below 200°C, marbles experienced minor brittle deformation, little documented by intercrystalline fractures, calcite veins, and fluid inclusions trails at a high angle to the main foliation. To which event this brittle deformation is connected is not immediately observable from our sampling. The onset of a brittle deformation toward the north and at the base of detachment has been already identify in the Kali Gandaki valley (Hurtado et al., 2001; Godin, 2003, with references). An example of this is the late brittle deformation that reactivated the Dhumpu Detachment, during a distinctive episode of late deformation in the Pliocene (Hurtado et al., 2001; McDermott et al., 2015; Pye et al., 2022).

With regard to the STDS *in sensu strictu*, we link the $D2_{early}$ deformation temperatures, strain rates and differential stress to the main detachment shearing and, more precisely, to the extensional juxtaposition of the hot GHS_U with the cold THS, and to the development of the pervasive mylonitic foliation and oblique foliation (Fig. 9). The following stage, where twinning dominated in the CPO reorientation ($D2_{late}$), occurred with a strain rates of c. 10^{-15} s^{-1}, which is still compatible to the strain rates observed though quartz paleopiezometry for the Everest area even in the main mylonitic zone (Law et al., 2011).

5.2. Tectonic implications for the Annapurna Detachment zone and the South Tibetan Detachment System

A temporal variation of the STDS internal deformation and rheology has been described for marbles and metalimestone in the Lower Dolpo Region (Nania et al., 2022b) and for quartz-mylonite in Eastern Himalaya (Long et al., 2019; Zhang et al., 2022). In central to eastern Himalaya, it has been suggested that this temporal variation occurred with a later localization of a brittle fault at shallower levels, with the same kinematics, merging into the ductile shear zone (Carosi et al., 1998; Searle et al., 2003; Searle, 2010, with references). The Qomolangma and Lhotse Detachment in the Everest area represent the best-preserved structures for this architecture (Carosi et al., 1998; Searle et al., 2003; Schultz et al., 2017). As in our case, an increase of differential stress overtime within the STDS has been documented implicitly in similar lithologies by Law et al. (2011). Values of 25–35 MPa are reported for a younger upper brittle segment of the STDS, whereas values of 10–15 MPa are documented for the older lower ductile shear zone in the Everest area.

The younger ductile-brittle to brittle normal-sense fault, however, crops out only in few other areas, especially in eastern Himalaya (e.g., Sikkim and Zhergerand, see Kellett et al., 2013; Montomoli et al., 2017, with references), lacking in several parts of the belt (Cottle et al., 2007; Kellett and Grujic, 2012; Carosi et al., 2013; Kellett et al., 2019 with references). Despite the occurrence of later normal-sense faults truncating (or close to) the mylonitic zone, like below the Phu Detachment in the Marsyandi valley, there is no conclusive evidence for the later localization of a brittle STDS segment where carbonate-bearing rocks are dominant, as in the Kali Gandaki valley, the Lower Dolpo region (Carosi et al., 2002, 2013), and the Manaslu range in Mid-Western Nepal.

For the Lower Dolpo region, the lack of the brittle fault at the top of the marble mylonite in the detachment zone has been recently correlated to the ability of calcite to deform plastically even at shallow crustal levels (Nania et al., 2022b). At temperatures below c. 300°C, quarzitic rocks would deform in the brittle regime, and the increasing strain hardening within the plastic-to-brittle shear zone would explain the migration and the new localization of the detachment, which is not required when marble mylonite are involved.

The structural data for the marble mylonites in the Annapurna Detachment zone support the same idea of a progressive evolution of the STDS without the localization of the upper branch (prior of possible late re-activations). The two main differences between the deformation path of the Annapurna Detachment zone and the one in Lower Dolpo concern the kinematic vorticity and the strain rate occurring during the $D2_{late}$. In the Lower Dolpo region, the strain rate remains constant from $D2_{early}$ to $D2_{late}$, while the kinematic vorticity recorded during the $D2_{late}$ is lower, locally suggesting a decelerating strain path (Nania et al., 2022b). We do not document, here, the same pattern in the Kali Gandaki valley, where the kinematic vorticity remained constant even when the plastic deformation rates decreased. Adopting our kinematic vorticity results, the shortening estimates of c. 13-14% (as a minimum estimate due to the used calcite crystals as strain markers) are still comparable with the values reported for the Everest area by Law et al. (2004) for the lower detachment (10-30%) and by Larson et al. (2020) for the upper detachment (14–26%). The variations between the Kali Gandaki valley, the Lower Dolpo region, as well as the other Himalayan areas, highlight the lateral variability of the regional structure, and stress the need for further investigations of other areas of the belt, through microstructural and interdisciplinary analyses on the mylonitic zone before building large-scale tectonic models.

6. Conclusion

Combining calcite microstructural analysis with regional-scale information, we reconstructed the evolution of the ductile Annapurna Detachment zone, representing the local segment of the Himalayan STDS in the Kali Gandaki valley. We documented:

- A progressive shallowing of the Annapurna Detachment zone occurred through two consecutive stages of ductile shearing ($D2_{early}$ and a $D2_{late}$), recorded by calcite microstructures. Mylonitic foliation, syn-kinematic mineral and calcite grain size developed during the $D2_{early}$, whereas calcite twinning, crosscutting most calcite grains and reorienting the calcite [*c*]-axes against the shear sense, occurred during the $D2_{late}$.
- The Annapurna Detachment zone suffered a cooling from the $D2_{early}$ (at least 500/550–400°C traced up-section) to the $D2_{late}$ (T≤250°C) under constant kinematic vorticity in a general shear flow. Strain rates probably decreased overtime from the $D2_{early}$ to the $D2_{late}$.
- We interpret these two stages of shearing as representative of a shallowing of the shear zone. Cooling of rocks at almost constant kinematic vorticity for little decelerations enhanced the increase in the differential stress and the strain hardening, accommodated by carbonates in the ductile regime.
- Compared the Annapurna Detachment zone to other segments of the STDS, we suggest that the regional-extended discontinuity did not experience an equal evolutionary history all along the Himalaya, with strain partitioning due to the different lithologies and local features. Protracted ductile shearing in carbonate-bearing rocks may be the cause of the lack of the upper brittle STDS in several Himalayan transects.
- From a broader point of view, our work highlights how the behaviour of marbles in shear zones can determine complex and composite histories, which can be deconvolved using calcite microfabrics.

Acknowledgements

We are grateful to Dr. Leiss and to all the staff at the Department of Structural Geology and Geodynamics at the Geoscience Centre of the Georg-August-University of Goettingen for their evaluable support during fabric analyses. We also thank Florian Duschl (Technical University Munich) for his help with cathodoluminescence analyses.

Author contributions

Laura Nania: Conceptualization; Data curation; Formal analysis; Methodology; Roles/Writing – original draft.

Chiara Montomoli: Field work and sample collections, Conceptualization; Methodology; Supervision; Funding acquisition; Project administration; Writing – review & editing.

Salvatore Iaccarino: Conceptualization; Methodology; Supervision; Funding acquisition; Writing – review & editing.

Rodolfo Carosi: Field work and sample collections, Conceptualization; Project administration; Writing – review & editing.

Funding

PRIN 2015 (University of Torino: R. Carosi and C. Montomoli) and Fondi ricerca locale (ex-60%) (University of Torino: S. Iaccarino, R. Carosi and C. Montomoli). This research is part of the Ph.D. project of LN funded by the Tuscany Regional Pegaso doctoral grant.

References

An, W., Hu, X., Garzanti, E., Wang, J. G., Liu, Q., 2021. New precise dating of the India-Asia collision in the Tibetan Himalaya at 61 Ma. Geophys. Res. 48(3), e2020GL090641. https://doi.org/10.1029/2020GL090641.

Axen, G.J., 2004. 3. Mechanics of Low-Angle Normal Faults, in: Karner, G., Taylor, B., Driscoll, N., Kohlstedt, D. (Eds.), Rheology and Deformation of the Lithosphere at Continental Margins. Columbia University Press, New York, pp. 46-91. https://doi.org/10.7312/karn12738-004.

Axen, G.J., 2020. How a strong low-angle normal fault formed: The Whipple detachment, southeastern California. Geol. Soc. Am. Bull. 132(9-10), 1817-1828. https://doi.org/10.1130/B35386.1.

Barnhoorn, A., Bystricky, M., Burlini, L., Kunze, K., 2004. The role of recrystallisation on the deformation behaviour of calcite rocks: large strain torsion experiments on Carrara marble. J. Struct. Geol. 26(5), 885-903. https://doi.org/10.1016/j.jsg.2003.11.024.

Barnhoorn, A., Bystricky, M., Burlini, L., Kunze, K., 2005. Post-deformational annealing of calcite rocks. Tectonophysics 403(1-4), 167-191. https://doi.org/10.1016/j.tecto.2005.04.008.

Bauer, H., Rogowitz, A., Grasemann, B., Decker, K., 2018. Intracrystalline deformation of calcite in the upper brittle crust. Geology 46(4), 375-378. https://doi.org/10.1130/G39990.1.

Beaumont, C., Jamieson, R.A., Nguyen, M.H., Lee, B., 2001. Himalayan tectonics explained by extrusion of a low-viscosity crustal channel coupled to focused surface denudation. Nature 414(6865), 738-742. https://doi.org/10.1038/414738a.

Beaumont, C., Jamieson, R. A., Nguyen, M. H., & Medvedev, S. (2004). Crustal channel flows: 1. Numerical models with applications to the tectonics of the Himalayan-Tibetan orogen. J. Geophys. Res. Solid Earth 109(B6), B06406. https://doi.org/10.1029/2003JB002809.

Bhandari, A., Jiang, D., 2021. A multiscale numerical modeling investigation on the significance of flow partitioning for the development of quartz c-axis fabrics. J. Geophys. Res. Solid Earth 126(2), e2020JB021040. https://doi.org/10.1029/2020JB021040.

Blisniuk, P. M., Hacker, B. R., Glodny, J., Ratschbacher, L., Bi, S., Wu, Z., McWilliams, M.O., Calvert, A., 2001) Normal faulting in central Tibet since at least 13.5 Myr ago. Nature 412(6847), 628-632. https://doi.org/10.1038/35088045.

Boggs, S., Krinsley, D., 2006. Application of cathodoluminescence imaging to the study of sedimentary rocks. Cambridge University Press, New York.

Bordet, P., Colchen, M., Krummenacher, D., Le Fort, P., Mouterde, R., Remy, M., 1971. Recherches géologiques dans l'Himalaya du Népal, région de la Thakkhola. Édition du Centre national de la recherche scientifique.

Brown, R.L., Nazarchuk, J.H., 1993. Annapurna Detachment fault in the Greater Himalaya of central Nepal. Geol. Soc. Spec. Publ. 74(1), 461-473. https://doi.org/10.1144/GSL.SP.1993.074.01.31.

Bunge, H.J., 1982. Texture analysis in materials science: mathematical methods, first ed. Butterworth-Heinemann, London.

Burchfiel, B.C., Royden, L.H., 1985. North-south extension within the convergent Himalayan region. Geology 13(10), 679-682. https://doi.org/10.1130/0091-7613(1985)13<679:NEWTCH>2.0.CO;2.

Burchfiel, B.C., Zhiliang, C., Hodges, K.V., Yuping, L., Royden, L.H., Changrong, D., 1992. The South Tibetan detachment system, Himalayan orogen: Extension contemporaneous with and parallel to shortening in a collisional mountain belt. Geol. Soc. Am. Spec. Pap. 269, 1-41. https://doi.org/10.1130/SPE269-p1.

Burg, J.P., Chen, G.M., 1984. Tectonics and structural zonation of southern Tibet, China. Nature 311, 219-223. https://doi.org/10.1038/311219a0.

Burkhard, M., 1993. Calcite twins, their geometry, appearance and significance as stress-strain markers and indicators of tectonic regime: a review. J. Struct. Geol. 15(3-5), 351-368. https://doi.org/10.1016/0191-8141(93)90132-T.

Busch, J. P., Van der Pluijm, B. A., 1995. Calcite textures, microstructures and rheological properties of marble mylonites in the Bancroft shear zone, Ontario, Canada. J. Struct. Geol. 17(5), 677-688. https://doi.org/10.1016/0191-8141(94)00092-E.

Caby, R., Pêcher, A., LeFort, P., 1983. The Himalayan Main Central Thrust: new data about the reverse metamorphism at the bottom of the Tibetan Slab. Rev. Geol. Dyn. Geogr. Phys. 24, 89-100.

Carosi, R., Gemignani, L., Godin, L., Iaccarino, S., Larson, K., Montomoli, C., Rai, S., 2014. A geological journey through the deepest gorge on Earth: The Kali Gandaki valley section, central Nepal, in: Montomoli, C., Carosi, R., Law, R., Singh, S., Rai, S.M. (Eds.), Geological field trips in the Himalaya, Karakoram and Tibet. J. Virtual Explor., Electronic Edition 1441-8142. https://doi.org/10.3809/Jvirtex.vol.2014.052.

Carosi, R., Lombardo, B., Molli, G., Musumeci, G., Pertusati, P.C., 1998. The South Tibetan detachment system in the Rongbuk valley, Everest region. Deformation features and geological implications. J. Asian Earth Sci. 16(2-3), 299-311. https://doi.org/10.1016/S0743-9547(98)00014-2.

Carosi, R., Montomoli, C., Iaccarino, S., 2018. 20 years of geological mapping of the metamorphic core across Central and Eastern Himalayas. Earth Sci. Rev. 177, 124-138. https://doi.org/10.1016/j.earscirev.2017.11.006.

Carosi, R., Montomoli, C., Iaccarino, S., Cottle, J.M., Massonne, H.J., Nania, L., Simonetti, M., 2023. Constraining the evolution of shear zones in the Himalayan mid crust in Central–Western Nepal: implications for the tectonic evolution of the Himalayan metamorphic core. Geol. Mag. https://doi.org/10.1017/S0016756823000365.

Carosi, R., Montomoli, C., Iaccarino, S., Massonne, H.J., Rubatto, D., Langone, A., Gemignani, L., Visonà, D., 2016. Middle to late Eocene exhumation of the Greater Himalayan Sequence in the Central Himalayas: Progressive accretion from the Indian plate. Bulletin 128(11-12), 1571-1592. https://doi.org/10.1130/B31471.1.

Carosi, R., Montomoli, C., Rubatto, D., Visonà, D., 2013. Leucogranite intruding the South Tibetan Detachment in western Nepal: implications for exhumation models in the Himalayas. Terra Nova 25(6), 478-489. https://doi.org/10.1111/ter.12062.

Carosi, R., Montomoli, C., Visonà, D., 2002. Is there any detachment in the Lower Dolpo (western Nepal)? CR. Geosci. 334(12), 933-940. https://doi.org/10.1016/S1631-0713(02)01828-X.

Carosi, R., Montomoli, C., Visonà, D., 2007. A structural transect in the Lower Dolpo: Insights on the tectonic evolution of Western Nepal. J. Asian Earth Sci. 29(2-3), 407-423. https://doi.org/10.1016/j.jseaes.2006.05.001.

Cawood, T.K., Platt, J.P., 2021. What controls the width of ductile shear zones?. Tectonophysics 816, 229033. https://doi.org/10.1016/j.tecto.2021.229033.

Chen, S., Zhang, B., Zhang, J., Wang, Y., Li, X., Zhang, L., Yan, Y., Cai, F., Yue, Y., 2022. Tectonic transformation from orogen-perpendicular to orogen-parallel extension in the North Himalayan Gneiss Domes: Evidence from a structural, kinematic, and geochronological investigation of the Ramba gneiss dome. J. Struct. Geol. 155, 104527. https://doi.org/10.1016/j.jsg.2022.104527.

Colchen, M., 1999. The Thakkhola–Mustang graben in Nepal and the late Cenozoic extension in the Higher Himalayas. J. Asian Earth Sci. 17(5-6), 683-702. https://doi.org/10.1016/S1367-9120(99)00037-1.

Colchen, M., Le Fort, P., Pecher. A., 1980. Carte geologique Annapurna- Manaslu- Ganesh, Himalaya du Nepal. Echelle 1:200.000. CNRS, Paris.

Colchen, M., Fort, P.L., Pêcher, A., 1986. Recherches géologiques dans l'Himalaya du Népal. Annapurna, Manaslu, Ganesh. CNRS, Paris.

Coleman, M.E., 1996. Orogen-parallel and orogen-perpendicular extension in the central Nepalese Himalayas. Geol. Soc. Am. Bull. 108(12), 1594-1607. https://doi.org/10.1130/0016-7606(1996)108<1594:OPAOPE>2.3.CO;2.

Corrie, S.L., Kohn, M.J., 2011. Metamorphic history of the central Himalaya, Annapurna region, Nepal, and implications for tectonic models. Geol. Soc. Am. Bull. 123(9-10), 1863-1879. https://doi.org/10.1130/B30376.1.

Corthouts, T.L., Lageson, D.R., Shaw, C.A., 2016. Polyphase deformation, dynamic metamorphism, and metasomatism of Mount Everest's summit limestone, east central Himalaya, Nepal/Tibet. Lithosphere 8(1), 38-57. https://doi.org/10.1130/L473.1.

Cottle, J.M., Jessup, M.J., Newell, D.L., Searle, M.P., Law, R.D., Horstwood, M.S., 2007. Structural insights into the early stages of exhumation along an orogen-scale detachment: the South Tibetan Detachment System, Dzakaa Chu section, Eastern Himalaya. J. Struct. Geol. 29(11), 1781-1797. https://doi.org/10.1016/j.jsg.2007.08.007.

Cottle, J.M., Waters, D. J., Riley, D., Beyssac, O., Jessup, M.J., 2011. Metamorphic history of the South Tibetan detachment system, Mt. Everest region, revealed by RSCM thermometry and phase equilibria modelling. J. Metamorph. Geol. 29, 561-582. https://doi.org/10.1111/j.1525-1314.2011.00930.x.

Crouzet, C., Dunkl, I., Paudel, L., Arkai, P., Rainer, T.M., Balogh, K., Appel, E., 2007. Temperature and age constraints on the metamorphism of the Tethyan Himalaya in Central Nepal: A multidisciplinary approach. J. Asian Earth Sci. 30(1), 113-130. https://doi.org/10.1016/j.jseaes.2006.07.014.

Daczko, N.R., Piazolo, S., 2022. Recognition of melferite–A rock formed in syn-deformational high-strain melt-transfer zones through sub-solidus rocks: A review and synthesis of microstructural criteria. Lithos 430-431, 106850. https://doi.org/10.1016/j.lithos.2022.106850.

De Bresser J.H.P., Spiers, C.J., 1993. Slip systems in calcite single crystals deformed at 300–800 C. J. Geophys. Res. Solid Earth 98(B4), 6397-6409. https://doi.org/10.1029/92JB02044.

De Bresser, J.H.P., Spiers, C.J., 1997. Strength characteristics of the r, f, and c slip systems in calcite. Tectonophysics 272(1), 1-23. https://doi.org/10.1016/S0040-1951(96)00273-9.

Ebert, A., Herwegh, M., Berger, A., Pfiffner, A., 2008. Grain coarsening maps for polymineralic carbonate mylonites: A calibration based on data from different Helvetic nappes (Switzerland). Tectonophysics 457(3-4), 128-142. https://doi.org/10.1016/j.tecto.2008.05.007.

Ebert, A., Herwegh, M., Evans, B., Pfiffner, A., Austin, N., Vennemann, T., 2007. Microfabrics in carbonate mylonites along a large-scale shear zone (Helvetic Alps). Tectonophysics 444(1-4), 1-26. https://doi.org/10.1016/j.tecto.2007.07.004.

Ebert, A., Rieke-Zapp, D., Herwegh, M., Ramseyer, K., Gnos, E., Decrouez, D., 2009. Microstructures of coarse-grained marbles, analyzed using a new technique based on the bireflectance of calcite. Tectonophysics 463(1-4), 175-184. https://doi.org/10.1016/j.tecto.2008.09.041.

Ferrill, D.A., 1998. Critical re-evaluation of differential stress estimates from calcite twins in coarse-grained limestone. Tectonophysics 285(1-2), 77-86. https://doi.org/10.1016/S0040-1951(97)00190-X.

Ferrill, D.A., Morris, A.P., Evans, M.A., Burkhard, M., Groshong Jr,R.H., Onasch, C.M., 2004. Calcite twin morphology: a low-temperature deformation geothermometer. J. Struct. Geol. 26(8), 1521-1529. https://doi.org/10.1016/j.jsg.2003.11.028.

Fossen, H., 2016. Structural Geology. Cambridge University Press, Cambridge.

Fossen, H., Cavalcante, G.C.G., 2017. Shear zones-A review. Earth Sci. Rev. 171, 434-455. https://doi.org/10.1016/j.earscirev.2017.05.002.

Fry, N., 1979. Random point distributions and strain measurement in rocks. Tectonophysics 60(1-2), 89-105. https://doi.org/10.1016/0040-1951(79)90135-5.

Fuchs, G., Frank, W., 1970. The geology of west Nepal between the rivers Kali Gandaki and Thulo Bheri. Jahrb. Der Geol. Bundesanstalt. 18, 1-103.

Garzanti, E., Gorza, M., Martellini, L., Nicora, A., 1994. Transition from diagenesis to metamorphism in the Paleozoic to Mesozoic succession of the Dolpo-Manang Synclinorium and Thakkhola Graben (Nepal Tethys Himalaya). Eclogae Geol. Helv. 87(2), 613-632. https://doi.org/10.5169/seals-167472.

Garzanti, E., Pagni Frette M., 1991. The stratigraphic succession of the Thakkhola region (central Nepal) - comparisons with the northwestern Tethys Himalaya. Riv. It. Paleont. Strat. 97. https://doi.org/10.13130/2039-4942/8980.

Garzanti, E., Vezzoli, G., Andò, S., Lavé, J., Attal, M., France-Lanord, C., DeCelles, P., 2007. Quantifying sand provenance and erosion (Marsyandi river, Nepal Himalaya). Earth Planet. Sci. Lett. 258(3-4), 500-515. https://doi.org/10.1016/j.epsl.2007.04.010.

Gemignani, L., van der Beek, P.A., Braun, J., Najman, Y., Bernet, M., Garzanti, E., Wijbrans, J.R., 2018. Downstream evolution of the thermochronologic age signal in the Brahmaputra catchment (eastern Himalaya): Implications for the detrital record of erosion. Earth Planet. Sci. Lett. 499, 48-61. https://doi.org/10.1016/j.epsl.2018.07.019.

Godin, L., 2003. Structural evolution of the Tethyan sedimentary sequence in the Annapurna area, central Nepal Himalaya. J. Asian Earth Sci. 22(4), 307-328. https://doi.org/10.1016/S1367-9120(03)00066-X.

Godin, L., Brown, R.L., Hanmer, S., Macfarlane, A., 1999a. High strain zone in the hanging wall of the Annapurna detachment, central Nepal Himalaya, in: Macfarlane, A., Sorkhabi, R.B., Quade, J. (Eds.), Himalaya and Tibet: Mountain Roots to Mountain Tops. Boulder, Colorado. Geol. Soc. Am. Spec. Pap. 328, 199-210. https://doi.org/10.1130/0-8137-2328-0.199.

Godin, L., Brown, R. L., Hanmer, S. Parrish, R., 1999b. Back folds in the core of the Himalayan orogen: An alternative interpretation. Geology 27(2), 151-154. https://doi.org/10.1130/0091-7613(1999)027<0151:BFITCO>2.3.CO;2.

Godin, L., Grujic, D., Law, R.D., Searle, M.P., 2006. Channel flow, ductile extrusion and exhumation in continental collision zones: an introduction. Geol. Soc. Spec. Publ. 268(1), 1-23. https://doi.org/10.1144/GSL.SP.2006.268.01.01.

Godin, L., Parrish, R.R., Brown, R.L., Hodges, K.V., 2001. Crustal thickening leading to exhumation of the Himalayan metamorphic core of central Nepal: Insight from U-Pb geochronology and 40Ar/39Ar thermochronology. Tectonics 20(5), 729-747. https://doi.org/10.1029/2000TC001204.

Govin, G., van der Beek, P., Najman, Y., Millar, I., Gemignani, L., Huyghe, P., Dupont-Nivet, G., Bernet, M., Mark, C., Wijbrans, J., 2020. Early onset and late acceleration of rapid exhumation in the Namche Barwa syntaxis, eastern Himalaya. Geology 48(12), 1139-1143. https://doi.org/10.1130/G47720.1.

Gradstein, F.M., Gibling, M.R., Sarti, M., Von Rad, U., Thurow, J.W., Ogg, J. G., Jansa, L.F., Kaminski, M.A., Westermann, G.E.G., 1991. Mesozoic Tethyan strata of Thakkhola, Nepal: evidence for the drift and breakup of Gondwana. Palaeogeogr. Palaeoclimatol. Palaeoecol. 88(3-4), 193-218. https://doi.org/10.1016/0031-0182(91)90065-Y.

Graziani, R., Larson, K.P., Soret, M., 2020. The effect of hydrous mineral content on competitive strain localization mechanisms in felsic granulites. J. Struct. Geol. 134, 104015. https://doi.org/10.1016/j.jsg.2020.104015.

Groshong Jr, R.H., 1988. Low-temperature deformation mechanisms and their interpretation. Geol. Soc. Am. Bull. 100(9), 1329-1360. https://doi.org/10.1130/0016-7606(1988)100<1329:LTDMAT>2.3.CO;2.

Grujic, D., Casey, M., Davidson, C., Hollister, L.S., Kündig, R., Pavlis, T., Schmid, S., 1996. Ductile extrusion of the Higher Himalayan Crystalline in Bhutan: evidence from quartz microfabrics. Tectonophysics 260(1-3), 21-43. https://doi.org/10.1016/0040-1951(96)00074-1.

Handy, M.R., 1994. Flow laws for rocks containing two non-linear viscous phases: a phenomenological approach. J. Struct. Geol. 16(3), 287-301. https://doi.org/10.1016/0191-8141(94)90035-3.

Herwegh, M., Berger, A., 2004. Deformation mechanisms in second-phase affected microstructures and their energy balance. J. Struct. Geol. 26(8), 1483-1498. https://doi.org/10.1016/j.jsg.2003.10.006.

Herwegh, M., Berger, A., Ebert, A., Brodhag, S., 2008. Discrimination of annealed and dynamic fabrics: consequences for strain localization and deformation episodes of large-scale shear zones. Earth Planet. Sci. Lett. 276(1-2), 52-61. https://doi.org/10.1016/j.epsl.2008.09.007.

Hielscher, R., Schaeben, H. 2008. A novel pole figure inversion method: specification of the MTEX algorithm. J. Appl. Crystallogr. 41(6), 1024-1037. https://doi.org/10.1107/S0021889808030112.

Hippertt, J.F., 1994. Microstructures and c-axis fabrics indicative of quartz dissolution in sheared quartzites and phyllonites. Tectonophysics 229, 141-163. https://doi.org/10.1016/0040-1951(94)90026-4.

Hodges, K.V., 2000. Tectonics of the Himalaya and southern Tibet from two perspectives. Geol. Soc. Am. Bull. 112(3), 324-350. https://doi.org/10.1130/0016-7606(2000)112<324:TOTHAS>2.0.CO;2.

Hodges, K.V., Parrish, R.R., Housh, T.B., Lux, D.R., Burchfiel, B.C., Royden, L.H., Chen, Z., 1992. Simultaneous Miocene extension and shortening in the Himalayan orogen. Science 258(5087), 1466-1470. https://doi.org/10.1126/science.258.5087.1466.

Hodges, K.V., Parrish, R.R., Searle, M.P., 1996. Tectonic evolution of the central Annapurna range, Nepalese Himalayas. Tectonics 15(6), 1264-1291. https://doi.org/10.1029/96TC01791.

Hu, X., Garzanti, E., Wang, J., Huang, W., An, W., Webb, A., 2016. The timing of India-Asia collision onset–Facts, theories, controversies. Earth Sci. Rev. 160, 264-299. https://doi.org/10.1016/j.earscirev.2016.07.014.

Hunter, N.J., Weinberg, R.F., Wilson, C.J.L., Luzin, V., Misra, S., 2019. Quartz deformation across interlayered monomineralic and polymineralic rocks: A comparative analysis. J. Struct. Geol. 119, 118-134. https://doi.org/10.1016/j.jsg.2018.12.005.

Huntington, K.W., Blythe, A.E., Hodges, K.V., 2006. Climate change and Late Pliocene acceleration of erosion in the Himalaya. Earth Planet. Sci. Lett. 252(1-2), 107-118. https://doi.org/10.1016/j.epsl.2006.09.031.

Hurtado Jr, J.M., Hodges, K.V., Whipple, K.X., 2001. Neotectonics of the Thakkhola graben and implications for recent activity on the South Tibetan fault system in the central Nepal Himalaya. Geol.

Soc. Am. Bull. 113(2), 222-240. https://doi.org/10.1130/0016-7606(2001)113<0222:NOTTGA>2.0.CO;2.

Iaccarino, S., Montomoli, C., Carosi, R., Massonne, H.J., Langone, A., Visonà, D., 2015. Pressure-temperature-time-deformation path of kyanite-bearing migmatitic paragneiss in the Kali Gandaki valley (Central Nepal): Investigation of Late Eocene-Early Oligocene melting processes. Lithos 231, 103-121. https://doi.org/10.1016/j.lithos.2015.06.005.

Iaccarino, S., Montomoli, C., Carosi, R., Montemagni, C., Massonne, H.J., Langone, A., Jain, A.K. and Visonà, D. 2017. Pressure-temperature-deformation-time constraints on the South Tibetan detachment system in the Garhwal Himalaya (NW India). Tectonics 36, 2281–2304. https://doi.org/10.1002/2017TC004566.

Iacopini, D., Carosi, R., Montomoli, C., Passchier, C.W., 2008. Strain analysis and vorticity of flow in the Northern Sardinian Variscan Belt: recognition of a partitioned oblique deformation event. Tectonophysics 446(1-4), 77-96. https://doi.org/10.1016/j.tecto.2007.10.002.

Jessup, M.J., Law, R.D., Searle, M.P., Hubbard, M.S., 2006. Structural evolution and vorticity of flow during extrusion and exhumation of the Greater Himalayan Slab, Mount Everest Massif, Tibet/Nepal: implications for orogen-scale flow partitioning. Geol. Soc. Spec. Publ. 268(1), 379-413. https://doi.org/10.1144/GSL.SP.2006.268.01.18.

Jessup, M.J., Newell, D.L., Cottle, J.M., Berger, A.L., Spotila, J.A., 2008. Orogen-parallel extension and exhumation enhanced by denudation in the trans-Himalayan Arun River gorge, Ama Drime Massif, Tibet-Nepal. Geology 36(7), 587-590. https://doi.org/10.1130/G24722A.1.

Jessup, M.J., Langille, J.M., Diedesch, T.F., Cottle, J.M., 2019. Gneiss dome formation in the Himalaya and southern Tibet. Geol. Soc. Spec. Publ. 483(1), 401-422. https://doi.org/10.1144/SP483.15.

Jiang, D., 1994a. Vorticity determination, distribution, partitioning and the heterogeneity and non-steadiness of natural deformations. J. Struct. Geol. 16(1), 121-130. https://doi.org/10.1016/0191-8141(94)90023-X.

Jiang, D., 1994b. Flow variation in layered rocks subjected to bulk flow of various kinematic vorticities: theory and geological implications. J. Struct. Geol. 16(8), 1159-1172. https://doi.org/10.1016/0191-8141(94)90059-0.

Jiang, D., Williams, P.F., 1999. A fundamental problem with the kinematic interpretation of geological structures. J. Struct. Geol. 21(8-9), 933-937. https://doi.org/10.1016/S0191-8141(99)00068-1.

Kellett, D.A., Cottle, J.M., Larson, K.P., 2019. The South Tibetan Detachment System: history, advances, definition and future directions. Geol. Soc. Spec. Publ. 483(1), 377-400. https://doi.org/10.1144/SP483.2.

Kellett, D.A., Grujic, D., 2012. New insight into the South Tibetan detachment system: Not a single progressive deformation. Tectonics 31, https://doi.org/10.1029/2011TC002957.

Kellett, D. A., Grujic, D., Coutand, I., Cottle, J., Mukul, M., 2013. The South Tibetan detachment system facilitates ultra rapid cooling of granulite-facies rocks in Sikkim Himalaya. Tectonics 32(2), 252-270. https://doi.org/10.1002/tect.20014.

Kern, H., Wenk, H.R., 1983. Calcite texture development in experimentally induced ductile shear zones. Contrib. to Mineral. Petrol. 83(3), 231-236. https://doi.org/10.1007/BF00371191.

Kilian, R., Heilbronner, R., 2017. Analysis of crystallographic preferred orientations of experimentally deformed Black Hills Quartzite. Solid Earth 8(5), 1095-1117. https://doi.org/10.5194/se-8-1095-2017.

Kilian, R., Heilbronner, R., Stünitz, H., 2011. Quartz microstructures and crystallographic preferred orientation: which shear sense do they indicate?. J. Struct. Geol. 33(10), 1446-1466. https://doi.org/10.1016/j.jsg.2011.08.005.

Kohn, M.J., 2008. PTt data from central Nepal support critical taper and repudiate large-scale channel flow of the Greater Himalayan Sequence. Geol. Soc. Am. 120(3-4), 259-273. https://doi.org/10.1130/B26252.1.

Lacombe, O., 2010. Calcite twins, a tool for tectonic studies in thrust belts and stable orogenic forelands. Oil & Gas Science and Technology – Rev. D'IFP Energies nouvelles 65(6), 809-838. https://doi.org/10.2516/ogst/2009088.

Lacombe, O., Parlangeau, C., Beaudoin, N.E., Amrouch, K., 2021. Calcite Twin Formation, Measurement and Use as Stress–Strain Indicators: A Review of Progress over the Last Decade. Geosciences 11(11), 445. https://doi.org/10.3390/geosciences11110445.

Lafrance, B., White, J.C., Williams, P.F., 1994. Natural calcite c-axis fabrics: an alternate interpretation. Tectonophysics 229(1-2), 1-18. https://doi.org/10.1016/0040-1951(94)90002-7.

Larson, K.P., Ambrose, T.K., Webb, A.A.G., Cottle, J.M., Shrestha, S., 2015. Reconciling Himalayan midcrustal discontinuities: the Main Central thrust system. Earth Planet. Sci. Lett. 429, 139-146. https://doi.org/10.1016/j.epsl.2015.07.070.

Larson, K.P., Graziani, R., Cottle, J.M., Apen, F., Corthouts, T., Lageson, D., 2020. The structural evolution of the Qomolangma Formation, Mount Everest, Nepal. J. Struct. Geol. 138, 104123. https://doi.org/10.1016/j.jsg.2020.104123.

Larson, K.P., Kellett, D.A., Cottle, J.M., Camacho, A., Brubacher, A.D., 2020. Mid-Miocene initiation of E-W extension and recoupling of the Himalaya. Terra Nova 32(2), 151-158. https://doi.org/10.1111/ter.12443.

Law, R.D., Jessup, M.J., Searle, M.P., Francsis, M.K., Waters, D.J., Cottle, J.M., 2011. Telescoping of isotherms beneath the South Tibetan detachment system, Mount Everest Massif. J. Struct. Geol. 33(11), 1569-1594. https://doi.org/10.1016/j.jsg.2011.09.004.

Law, R.D., Searle, M.P., Simpson, R.L., 2004. Strain, deformation temperatures and vorticity of flow at the top of the Greater Himalayan Slab, Everest Massif, Tibet. J. Geol. Soc. London 161(2), 305-320. https://doi.org/10.1144/0016-764903-047.

Leiss, B., Molli, G. 2003. 'High-temperature'texture in naturally deformed Carrara marble from the Alpi Apuane, Italy. J. Struct. Geol. 25(4), 649-658. https://doi.org/10.1016/S0191-8141(02)00148-7.

Leiss, B., Ullemeyer, K., 2006. Neue Perspektiven der Texturanalytik von Gesteinenmit konventioneller Röntgenbeugung., in: Philipp, S.L., Leiss, B., Vollbrecht, A., Tanner, D., Gudmundsson, A. (Eds.), 11. Symposium. Tektonik, Struktur und Kristallingeologie, Göttingen: Universitätsverlag, 128-130. https://doi.org/10.23689/fidgeo-1930.

Lister, G.S. 1977. Discussion: crossed-girdle c-axis fabrics in quartzites plastically deformed by plane strain and progressive simple shear. Tectonophysics 39(1-3), 51-54. https://doi.org/10.1016/0040-1951(77)90087-7.

Long, S.P., Mullady, C.L., Starnes, J.K., Gordon, S.M., Larson, K.P., Pianowski, L.S., Miller, R.B., Soignard, E., 2019. A structural model for the South Tibetan detachment system in northwestern Bhutan from integration of temperature, fabric, strain, and kinematic data. Lithosphere 11(4), 465-487. https://doi.org/10.1130/L1049.1.

Lopez-Sanchez, M.A., Llana-Fúnez, S., 2015. An evaluation of different measures of dynamically recrystallized grain size for paleopiezometry or paleowattometry studies. Solid Earth 6(2), 475-495. https://doi.org/10.5194/se-6-475-2015.

McDermott, J.A., Hodges, K.V., Whipple, K.X., Van Soest, M.C., Hurtado Jr, J.M., 2015. Evidence for Pleistocene low-angle normal faulting in the Annapurna-Dhaulagiri Region, Nepal. J. Geol. 123(2), 133-151. https://doi.org/10.1086/681219.

Mitsuishi, M., Wallis, S.R., Aoya, M., Lee, J., Wang, Y., 2012. E–W extension at 19 Ma in the Kung Co area, S. Tibet: Evidence for contemporaneous E–W and N–S extension in the Himalayan orogen. Earth Planet. Sci. Lett. 325, 10-20. https://doi.org/10.1016/j.epsl.2011.11.013.

Molli, G., Conti, P., Giorgetti, G., Meccheri, M., Oesterling, N. 2000. Microfabric study on the deformational and thermal history of the Alpi Apuane marbles (Carrara marbles), Italy. J. Struct. Geol. 22(11-12), 1809-1825. https://doi.org/10.1016/S0191-8141(00)00086-9.

Molli, G., Cortecci, G., Vaselli, L., Ottria, G., Cortopassi, A., Dinelli, E,ì., Mussi, M., Barbieri, M., 2010. Fault zone structure and fluid–rock interaction of a high angle normal fault in Carrara marble (NW Tuscany, Italy). J. Struct. Geol. 32(9), 1334-1348. https://doi.org/10.1016/j.jsg.2009.04.021.

Molli, G., Heilbronner, R., 1999. Microstructures associated with static and dynamic recrystallization of Carrara marble (Alpi Apuane, NW Tuscany, Italy). Geologie en Mijnbouw 78(1), 119-126.

Molli, G., White, J.C., Kennedy, L., Taini, V., 2011. Low-temperature deformation of limestone, Isola Palmaria, northern Apennine, Italy–The role of primary textures, precursory veins and intracrystalline deformation in localization. J. Struct. Geol. 33(3), 255-270. https://doi.org/10.1016/j.jsg.2010.11.015.

Montomoli, C., Carosi, R., Rubatto, D., Visonà, D., Iaccarino, S., 2017. Tectonic activity along the inner margin of the South Tibetan Detachment constrained by syntectonic leucogranite emplacement in Western Bhutan. Ital. J. Geosci. 136(1), 5-14. https://doi.org/10.3301/IJG.2015.26.

Morales, L.F., Lloyd, G.E., Mainprice, D., 2014. Fabric transitions in quartz via viscoplastic self-consistent modeling part I: Axial compression and simple shear under constant strain. Tectonophysics 636, 52-69. https://doi.org/10.1016/j.tecto.2014.08.011.

Morales, L.F., Mainprice, D., Lloyd, G.E., Law, R.D., 2011. Crystal fabric development and slip systems in a quartz mylonite: an approach via transmission electron microscopy and viscoplastic self-consistent modelling. Geol. Soc. Spec. Publ. 360(1), 151-174. https://doi.org/10.1144/SP360.9.

Murphy, M.A., Yin, A., Kapp, P., Harrison, T.M., Manning, C.E., Ryerson, F.J., Lin, D., Jinghui, G., 2002. Structural evolution of the Gurla Mandhata detachment system, southwest Tibet: Implications for the eastward extent of the Karakoram fault system. Geol. Soc. Am. Bull. 114(4), 428-447. https://doi.org/10.1130/0016-7606(2002)114<0428:SEOTGM>2.0.CO;2.

Nagy, C., Godin, L., Antolín, B., Cottle, J., Archibald, D., 2015. Mid-Miocene initiation of orogen-parallel extension, NW Nepal Himalaya. Lithosphere 7(5), 483-502. https://doi.org/10.1130/L425.1.

Nania, L., Montomoli, C., Iaccarino, S., Di Vincenzo, G., Carosi, R., 2022a. A thermal event in the Dolpo region (Nepal): a consequence of the shift from orogen perpendicular to orogen parallel extension in central Himalaya? J. Geol. Soc. London 179(1). https://doi.org/10.1144/jgs2020-261.

Nania, L., Montomoli, C., Iaccarino, S., Leiss, B., Carosi, R., 2022b. Multi-stage evolution of the South Tibetan Detachment System in central Himalaya: Insights from carbonate-bearing rocks. J. Struct. Geol. 158, 104574. https://doi.org/10.1016/j.jsg.2022.104574.

Negrini, M., Smith, S.A., Scott, J.M., Tarling, M.S., 2018. Microstructural and rheological evolution of calcite mylonites during shear zone thinning: Constraints from the Mount Irene shear zone, Fiordland, New Zealand. J. Struct. Geol. 106, 86-102. https://doi.org/10.1016/j.jsg.2017.11.013.

Oesterling, N., Heilbronner, R., Stünitz, H., Barnhoorn, A., Molli, G., 2007. Strain dependent variation of microstructure and texture in naturally deformed Carrara marble. J. Struct. Geol. 29(4), 681-696. https://doi.org/10.1016/j.jsg.2006.10.007.

Ohl, M., Nzogang, B., Mussi, A., Wallis, D., Drury, M., Plümper, O., 2021. Crystal-Plastic Deformation in Seismically Active Carbonate Fault Rocks. J. Geophys. Res. Solid Earth 126(4), e2020JB020626. https://doi.org/10.1029/2020JB020626.

Olgaard, D.L., 1990. The role of second phase in localizing deformation. Geol. Soc. Spec. Publ. 54(1), 175-181. https://doi.org/10.1144/GSL.SP.1990.054.01.17.

Parlangeau, C., Lacombe, O., Schueller, S., Daniel, J.M., 2018. Inversion of calcite twin data for paleostress orientations and magnitudes: A new technique tested and calibrated on numerically-generated and natural data. Tectonophysics 722, 462-485. https://doi.org/10.1016/j.tecto.2017.09.023.

Parsons, A.J., Ferré, E.C., Law, R.D., Lloyd, G.E., Phillips, R.J., Searle, M.P., 2016a. Orogen-parallel deformation of the Himalayan midcrust: Insights from structural and magnetic fabric analyses of the Greater Himalayan Sequence, Annapurna-Dhaulagiri Himalaya, central Nepal. Tectonics 35(11), 2515-2537. https://doi.org/10.1002/2016TC004244.

Parsons, A.J., Hosseini, K., Palin, R., Sigloch, K., 2020. Geological, geophysical and plate kinematic constraints for models of the India-Asia collision and the post-Triassic central Tethys oceans. Earth Sci. Rev. 103084, https://doi.org/10.1016/j.earscirev.2020.103084.

Parsons, A.J., Law, R.D., Lloyd, G.E., Phillips, R.J., Searle, M.P., 2016b. Thermo-kinematic evolution of the Annapurna-Dhaulagiri Himalaya, central Nepal: The Composite Orogenic System. Geochem. Geophys. Geosyst. 17(4), 1511-1539. https://doi.org/10.1002/2015GC006184.

Parsons, A.J., Law, R.D., Searle, M.P., Phillips, R.J., Lloyd, G.E., 2016c. Geology of the Dhaulagiri-Annapurna-Manaslu Himalaya, Western Region, Nepal. 1: 200,000. J. Map 12(1), 100-110. https://doi.org/10.1080/17445647.2014.984784.

Parsons, A.J., Phillips, R.J., Lloyd, G.E., Law, R.D., Searle, M.P., Walshaw, R.D., 2016d. Mid-crustal deformation of the Annapurna-Dhaulagiri Himalaya, central Nepal: An atypical example of channel flow during the Himalayan orogeny. Geosphere 12(3), 985-1015. https://doi.org/10.1130/GES01246.1.

Passchier, C.W., 1997. The fabric attractor. J. Struct. Geol. 19(1), 113-127. https://doi.org/10.1016/S0191-8141(96)00077-6.

Passchier, C.W. Trouw, R.A., 2005. Microtectonics, 2nd Revised and Enlarged Edition. Springer Science Business Media, Würzburg. https://doi.org/10.1007/3-540-29359-0.

Pêcher, A., 1978. Déformations et Metamorphisme Associés à une Zone de Cisaillement, Exemple du Grand Chevauchement Central Himalayen (MCT), Transversale des Annapurnas et du Manaslu, Népal [Ph.D. thesis]. Université de Grenoble, Grenoble.

Piazolo S., Passchier C.W., 2002. Controls on lineation development in low to medium grade shear zones: a study from the Cap de Creus peninsula, NE Spain. J. Struct. Geol. 24, 25-44. https://doi.org/10.1016/S0191-8141(01)00045-1.

Pye, A.E., Hodges, K.V., Keller, C.B., Law, R.D., van Soest, M.C., Bhandari, B., McDonald, C.S., 2022. Prolonged Slip on the South Tibetan Detachment Constrains Tectonic Models for Synorogenic Extension in the Central Himalaya. Tectonics 41(11), e2022TC007298. https://doi.org/10.1029/2022TC007298.

Renner, J., Evans, B., Siddiqi, G., 2002. Dislocation creep of calcite. J. Geophys. Res. Solid Earth 107(B12), ECV-6. https://doi.org/10.1029/2001JB001680.

Roger, F., Calassou, S., Lancelot, J., Malavieille, J., Mattauer, M., Zhiqin, X., Ziwen, H., Liwei, H., 1995. Miocene emplacement and deformation of the Konga Shan granite (Xianshui He fault zone, west Sichuan, China): Geodynamic implications. Earth Planet. Sci. Lett. 130(1-4), 201-216. https://doi.org/10.1016/0012-821X(94)00252-T.

Rogowitz, A., Grasemann, B., Huet, B., Habler, G., 2014. Strain rate dependent calcite microfabric evolution–An experiment carried out by nature. J. Struct. Geol. 69, 1-17. https://doi.org/10.1016/j.jsg.2014.08.004.

Rogowitz, A., White, J.C., Grasemann, B., 2016. Strain localization in ultramylonitic marbles by simultaneous activation of dislocation motion and grain boundary sliding (Syros, Greece). Solid Earth 7(2), 355-366. https://doi.org/10.5194/se-7-355-2016.

Rowe, K.J., Rutter, E.H., 1990. Palaeostress estimation using calcite twinning: experimental calibration and application to nature. J. Struct. Geol. 12(1), 1-17. https://doi.org/10.1016/0191-8141(90)90044-Y.

Rutter, E.H., 1974. The influence of temperature, strain rate and interstitial water in the experimental deformation of calcite rocks. Tectonophysics 22(3-4), 311-334. https://doi.org/10.1016/0040-1951(74)90089-4.

Rybacki, E., Janssen, C., Wirth, R., Chen, K., Wenk, H.R., Stromeyer, D., Dresen, G., 2011. Low-temperature deformation in calcite veins of SAFOD core samples (San Andreas Fault)—microstructural analysis and implications for fault rheology. Tectonophysics 509(1-2), 107-119. https://doi.org/10.1016/j.tecto.2011.05.014.

Sarkarinejad, K., Heibati, Z., 2017. Vorticity analysis in the Zagros orogen, Shiraz area, Iran. Int. J. Earth Sci. 106(6), 2041-2065. https://doi.org/10.1007/s00531-016-1411-3.

Schaeben, H. 1997. A simple standard orientation density function: The hyperspherical de la Vallée Poussin kernel. Phys. Status Solidi (B) 200(2), 367-376. https://doi.org/10.1002/1521-3951(199704)200:2<367::AID-PSSB367>3.0.CO;2-I.

Schenk, O., Urai, J.L., Evans, B., 2005. The effect of water on recrystallization behavior and grain boundary morphology in calcite–observations of natural marble mylonites. J. Struct. Geol. 27(10), 1856-1872. https://doi.org/10.1016/j.jsg.2005.05.015.

Schmid, S.M., Casey, M., 1986. Complete fabric analysis of some commonly observed quartz c-axis patterns. Geophys. Monogr. Ser. 36, 263-286. https://doi.org/10.1029/GM036p0263.

Schmid, S.M., Panozzo, R., Bauer, S., 1987. Simple shear experiments on calcite rocks: rheology and microfabric. J. Struct. Geol. 9(5-6), 747-778. https://doi.org/10.1016/0191-8141(87)90157-X.

Schneider, C., Masch, L., 1993. The metamorphism of the Tibetan series from the Manang area, Marsyandi valley, central Nepal. Geol. Soc. Spec. Publ. 74(1), 357-374. https://doi.org/10.1144/GSL.SP.1993.074.01.24.

Schultz, M.H., Hodges, K.V., Ehlers, T.A., Van Soest, M., Wartho, J.A., 2017. Thermochronologic constraints on the slip history of the South Tibetan detachment system in the Everest region, southern Tibet. Earth Planet. Sci. Lett. 459, 105-117. https://doi.org/10.1016/j.epsl.2016.11.022.

Searle, M.P., 1999. Extensional and compressional faults in the Everest–Lhotse massif, Khumbu Himalaya, Nepal. J. Geol. Soc. London 156(2), 227-240, https://doi.org/10.1144/gsjgs.156.2.0227.

Searle, M.P., 2010. Low-angle normal faults in the compressional Himalayan orogen; Evidence from the Annapurna–Dhaulagiri Himalaya, Nepal. Geosphere 6(4), 296-315. https://doi.org/10.1130/GES00549.1.

Searle, M.P., Simpson, R.L., Law, R.D., Parrish, R.R., Waters, D.J., 2003. The structural geometry, metamorphic and magmatic evolution of the Everest massif, High Himalaya of Nepal-South Tibet. J. Geol. Soc. London 160(3), 345-366. https://doi.org/10.1144/0016-764902-126.

Simpson, C., Paor, D.G.D., 1997. Practical analysis of general shear zones using the porphyroclast hyperbolic distribution method: an example from the Scandinavian Caledonides, in: Sengupta, S. (Ed.), Evolution of geological structures in micro-to macro-scales. Chapman & Hall, London, pp. 169-184. https://doi.org/10.1007/978-94-011-5870-1_10.

Skemer, P., Katayama, I., Jiang, Z., Karato, S.I., 2005. The misorientation index: Development of a new method for calculating the strength of lattice-preferred orientation. Tectonophysics 411(1-4), 157-167. https://doi.org/10.1016/j.tecto.2005.08.023.

Sly, M.K., Thind, A.S., Mishra, R., Flores, K.M., Skemer, P., 2020. Low-temperature rheology of calcite. Geophys. J. Int. 221(1), 129-141. https://doi.org/10.1093/gji/ggz577.

Soucy La Roche, R., Godin, L., Cottle, J.M., Kellett, D.A., 2018. Preservation of the early evolution of the Himalayan middle crust in foreland klippen: Insights from the Karnali klippe, west Nepal. Tectonics 37(5), 1161-1193. https://doi.org/10.1002/2017TC004847.

Spanos, D., Xypolias, P., Koukouvelas, I., 2015. Vorticity analysis in calcite tectonites: An example from the Attico-Cycladic massif (Attica, Greece). J. Struct. Geol. 80, 120-132. https://doi.org/10.1016/j.jsg.2015.08.014.

Stallard, A., Shelley, D., 1995. Quartz c-axes parallel to stretching directions in very low-grade metamorphic rocks. Tectonophysics 249(1-2), 31-40. https://doi.org/10.1016/0040-1951(95)00040-T.

Stipp, M., Tullis, J., 2003. The recrystallized grain size piezometer for quartz. Geophys. Res. 30(21), 2088, https://doi.org/10.1029/2003GL018444.

Stipp, M., Stünitz, H., Heilbronner, R., Schmid, S.M., 2002. The eastern Tonale fault zone: a 'natural laboratory' for crystal plastic deformation of quartz over a temperature range from 250 to 700 °C. J. Struct. Geol. 24(12), 1861-1884. https://doi.org/10.1016/S0191-8141(02)00035-4.

Streule, M.J., Searle, M.P., Waters, D.J., Horstwood, M.S., 2010. Metamorphism, melting, and channel flow in the Greater Himalayan Sequence and Makalu leucogranite: Constraints from thermobarometry, metamorphic modeling, and U-Pb geochronology. Tectonics 29(5), TC5011. https://doi.org/10.1029/2009TC002533.

Toy, V.G., Prior, D.J., Norris, R.J., 2008. Quartz fabrics in the Alpine Fault mylonites: Influence of pre-existing preferred orientations on fabric development during progressive uplift. J. Struct. Geol. 30(5), 602-621. https://doi.org/10.1016/j.jsg.2008.01.001.

Tripathy, V., Saha, D., 2015. Inversion of calcite twin data, paleostress reconstruction and multiphase weak deformation in cratonic interior–Evidence from the Proterozoic Cuddapah basin, India. J. Struct. Geol. 77, 62-81. https://doi.org/10.1016/j.jsg.2015.05.009.

Tullis, J., Wenk, H.R., 1994. Effect of muscovite on the strength and lattice preferred orientations of experimentally deformed quartz aggregates. Mater. Sci. Eng. A. 175(1-2), 209-220. https://doi.org/10.1016/0921-5093(94)91060-X.

Ulrich, S., Schulmann, K., Casey, M., 2002. Microstructural evolution and rheological behaviour of marbles deformed at different crustal levels. J. Struct. Geol. 24(5), 979-995. https://doi.org/10.1016/S0191-8141(01)00132-8.

US National Institutes of Health, Bethesda, Maryland, USA, 2016. ImageJ (Version 1.53t). https://imagej.nih.gov/ij/download.html (accessed 24 November 2022).

Vannay, J.C., Grasemann, B., 2001. Himalayan inverted metamorphism and syn-convergence extension as a consequence of a general shear extrusion. Geol. Mag. 138(3), 253-276. https://doi.org/10.1017/S0016756801005313.

Vannay, J.C., Hodges, K.V., 1996. Tectonometamorphic evolution of the Himalayan metamorphic core between the Annapurna and Dhaulagiri, central Nepal. J. Metamorph. Geol. 14(5), 635-656. https://doi.org/10.1046/j.1525-1314.1996.00426.x.

Verberne, B. A., Spiers, C. J., Niemeijer, A. R., De Bresser, J. H. P., De Winter, D. A. M., Plümper, O., 2014. Frictional properties and microstructure of calcite-rich fault gouges sheared at sub-seismic sliding velocities. Pure Appl. Geophys. 171, 2617-2640. https://doi.org/10.1007/s00024-013-0760-0.

Visonà, D., Lombardo, B., 2002. Two-mica and tourmaline leucogranites from the Everest–Makalu region (Nepal–Tibet). Himalayan leucogranite genesis by isobaric heating? Lithos 62(3-4), 125-150. https://doi.org/10.1016/S0024-4937(02)00112-3.

Visonà, D., Carosi, R., Montomoli, C., Tiepolo, M., Peruzzo, L., 2012. Miocene andalusite leucogranite in central-east Himalaya (Everest–Masang Kang area): low-pressure melting during heating. Lithos 144, 194-208. https://doi.org/10.1016/j.lithos.2012.04.012.

Waldron, J.W., Wallace, K.D., 2007. Objective fitting of ellipses in the centre-to-centre (Fry) method of strain analysis. J. Struct. Geol. 29(9), 1430-1444. https://doi.org/10.1016/j.jsg.2007.06.005.

Wallis, S., 1995. Vorticity analysis and recognition of ductile extension in the Sanbagawa belt, SW Japan. J. Struct. Geol. 17(8), 1077-1093. https://doi.org/10.1016/0191-8141(95)00005-X.

Wallis, S.R., Platt, J.P., Knott, S.D., 1993. Recognition of syn-convergence extension in accretionary wedges with examples from the Calabrian Arc and the Eastern Alps. Am. J. Sci. 293(5), 463-494. https://doi.org/10.2475/ajs.293.5.463.

Waters, D.J., 2019. Metamorphic constraints on the tectonic evolution of the High Himalaya in Nepal: the art of the possible. Geol. Soc. Spec. Publ. 483(1), 325-375. https://doi.org/10.1144/SP483-2018-187.

Waters, D.J., Law, R.D., Searle, M.P., Jessup, M.J., 2019. Structural and thermal evolution of the South Tibetan Detachment shear zone in the Mt Everest region, from the 1933 sample collection of LR Wager. Geol. Soc. Spec. Publ. 478(1), 335-372. https://doi.org/10.1144/SP478.17.

Webb, A.A.G., Yin, A., Harrison, T.M., Célérier, J., Burgess, W.P., 2007. The leading edge of the Greater Himalayan Crystalline complex revealed in the NW Indian Himalaya: Implications for the evolution of the Himalayan orogen. Geology 35(10), 955-958. https://doi.org/10.1130/G23931A.1.

Wenk, H.R., Takeshita, T., Bechler, E., Erskine, B.G., Matthies, S., 1987. Pure shear and simple shear calcite textures. Comparison of experimental, theoretical and natural data. J. Struct. Geol. 9(5-6), 731-745. https://doi.org/10.1016/0191-8141(87)90156-8.

Whitney, D.L., Evans, B.W., 2010. Abbreviations for names of rock-forming minerals. Am. Mineral. 95(1), 185-187. https://doi.org/10.2138/am.2010.3371.

Xypolias, P., 2010. Vorticity analysis in shear zones: a review of methods and applications. J. Struct. Geol. 32(12), 2072-2092. https://doi.org/10.1016/j.jsg.2010.08.009.

Yin, A., 2006. Cenozoic tectonic evolution of the Himalayan orogen as constrained by along-strike variation of structural geometry, exhumation history, and foreland sedimentation. Earth Sci. Rev. 76(1-2), 1-131. https://doi.org/10.1016/j.earscirev.2005.05.004.

Zhang, L., Zhang, B., Zhang, J., Wang, J., Cai, F., Zhao, Z., Chen, S., Li, X., 2022. The rheology and deformation of the South Tibetan Detachment System as exposed at Zherger La, east-central Himalaya: Implications for exhumation of the Himalayan metamorphic core. J. Struct. Geol. 157, 104559. https://doi.org/10.1016/j.jsg.2022.104559.

Zhang, L.K., Li, G.M., Cao, H.W., Zhang, Z., Dong, S.L., Liang, W., Fu, J.G., Huang, Y., Xia, X.B., Dai, Z.W., Pei, Q.M., Zhang, S.T., 2020. Activity of the south Tibetan detachment system: Constraints from leucogranite ages in the eastern Himalayas. Geol. J. 55(7), 5540-5573. https://doi.org/10.1002/gj.3756.

Figure and Table Captions

Fig. 1 – Geological map of the Nepal Himalaya, modified after Corrie and Kohn (2011). The location of the Kali Gandaki valley is highlighted. Abbreviations: HHL, High Himalayan Leucogranite; THS, Tethyan Himalayan Sequence; GHS, Greater Himalayan Sequence; LHS, Lesser Himalayan Sequence; SHS, Subhimalayan Sequence; MCT: Main Central Thrust; STDS: South Tibetan Detachment System; MBT: Main Boundary Thrust; MFT: Main Frontal Thrust.

Fig. 2 – (a) Upper Kali Gandaki valley geological sketch map (modified after Godin, 2003 and Carosi et al., 2016) showing the originally mapped Annapurna Detachment (AD) as solid line, the inferred high-strain zone boundaries by the dashed lines, and study sample's location as yellow dots. The GHS_U Unit definition follows Godin (2003). **(b)** S-N geological cross section from Lete toward Marpha (A-A' trace in a).

Fig. 3 – Micro photos (crossed nicols) of representative samples referred to their structural position with respect to the S-N geological cross section. The red solid line (AD) indicates the Annapurna Detachment's position according to Godin et al. (1999a). **(a)** Massive limestone from the Nilgiri Fm. (THS), with serrated calcite grain boundaries typical of pressure solution processes. **(b)** Impure marble with oblique SPO, lobate boundaries, and twins in calcite. Coarse-grained biotite crosscuts the main foliation. **(c-d)** Marbles with calcite lobate grain boundaries, oblique SPO, and Type II *e*-twins. **(e)** Photos of sample K21-10-18 under optical microscope and in hot-cathodoluminescence (insert). **(f-i)** Coarse-grained marbles within the GHS_U. **(j)** Straight grain boundaries in the coarse-grained calcite within the GHS_U.

Fig. 4 – Key images of part of the grain size distribution maps acquired for the analysed sample. Images are only part of the grain size distribution maps to allow an immediate comparison between samples for the same scale. Cal% is the measured 2D abundance of calcite in each sample. The vertical scalebar on the left of each map correspond to the equivalent radius of each grain calculated by ImageJ software. White hole are the second-phase minerals. The main grain size distribution histograms are plotted for representative samples. See Table 2 for details.

Fig. 5 – Examples of analysed twin sets in calcite crystals used for paleopiezometry and paleothermometry estimations. **(a)** annealed boundaries of untwined crystals are indicated. **(b)** Example of high-angle boundaries due to twinning, leading to pressure solution processes. The white arrow points tapered twins. **(c)** Mean twin width vs mean twin density plot after Ferrill et al. (2004). The dashed blue and orange curves indicate paths of increasing strain for temperatures below 170°C and above 200°C, respectively. The main twin sets point out final temperature conditions of 170-200 °C, while the preserved tapered and thicker twins support deformation temperatures above 200 °C.

Fig. 6 – Main quartz (**a-c**) and calcite (**d-h**) pole figures (the specimens are listed from top to bottom along the profile, reference frame is displayed at the top left). Pole figures shows that both quartz and calcite CPO are well-defined, supporting asymmetric fabrics. See text for further details.

Fig. 7 – (a) Wenk et al. (1987) diagram for estimating simple shear contribution in marbles from calcite CPOs. **(b)** adapted Law et al. (2004) graph for kinematic vorticity estimates obtained from both applied methods. Relationship between kinematic vorticity and relative components of pure and simple shear for instantaneous 2D flow is given. See Table 3 for details.

Fig. 8 – Fry plot with interpreted fabric ellipse. Low-density areas (vacancy field ellipse) approximate the finite strain equivalent ellipse. Voids are defined through the exponential edge detection method of Waldron and Wallace (2007). Rxz = Finite strain axial ratios for XZ sections of finite strain ellipsoid.

Fig. 9 – Schematic illustration for the Annapurna Detachment zone tectonic evolution, compared for a crustal strength/differential stress profile (not to scale). The black solid line refers to the strain rate at the $D2_{early}$, whereas the dashed line refers to the $D2_{late}$. Two main stages of shallowing and cooling, $D2_{early}$ (a) and $D2_{late}$ (b) are suggested for decreasing strain rates under subsimple shear, supporting a strain hardening and an increase of the differential stress.

Table 1

Sample	Latitude, longitude	Formation (Unit)	Mineral Assemblage	Calcite deformation	Analysis	Fabric
K21-10-05	28.735472, 83.677528	Sombre Fm. (THS)	Cal+Qz+Wm	pressure solution	◔	Isotropic coarse-grained limestone
K21-10-12A	28.699472, 83.625917	Annapurna Fm. (THS)	Cal+Dol+Qz+Wm+Bt±Chl	SGR + twinning	●	Continuous foliation (Sp), Calcite SPO
K21-10-12	28.699472, 83.625917	Annapurna Fm. (THS)	Cal+Dol+Qz+Wm±Rt	GBM + twinning	●	Continuous foliation (Sp), Calcite SPO
K21-10-13	28.699472, 83.625917	Annapurna Fm. (THS)	Cal+Dol+Qz+Wm+Bt±Chl	GBM + twinning	◔	Continuous foliation (Sp), Calcite SPO
K21-10-18	28.666917, 83.590472	Annapurna Fm. (THS)	Cal+Dol+Qz+Kfs±Bt±Wm±Chl	GBM + twinning	◐	Continuous foliation (Sp), Calcite SPO
K22-10-19	28.672250, 83.597306	Annapurna Fm. (THS)	Cal+Dol+Qz+Bt+Wm	GBM + twinning	●	Continuous foliation (Sp)
K29-10-51	28.650333, 83.626722	Unit III (GHS_U)	Cal Dol+Qz+Bt	GBM + twinning	◔	Continuous foliation (Sp)
K29-10-52	28.650333, 83.626722	Unit III (GHS_U)	Cal+Dol+Qz+Bt	GBM + twinning	●	Continuous foliation (Sp)
K29-10-53	28.650333, 83.626722	Unit III (GHS_U)	Cal+Dol+Qz+Bt	GBM + twinning	◔	Continuous foliation (Sp)
K31-10-64	28.666306, 83.588639	Unit III (GHS_U)	Cal+Dol+Qz+Bt	GBM + twinning	◕	Continuous foliation (Sp), Calcite SPO
K31-10-65	28.666306, 83.588639	Unit III (GHS_U)	Cal+Dol+Qz+Bt	GBM + static recrystallization	◕	Continuous foliation (Sp), Calcite SPO

Legend: ○ microstructural analysis; ◔ paleopiezometry; ◒ Finite-strain analysis; ◐ CPO.

Table 1 – Summary of the studied samples structural positions, features, and related type of analysis. Abbreviations: Bt – biotite; Cal – calcite; Chl – chlorite; Dol – dolomite; Kfs – feldspar; Qz – quartz; Rt – rutile; Wm – white mica; GBM – grain boundary migration; SGR – subgrain rotation recrystallization; Sp – main foliation; SPO – shape preferred orientation.

Table 2

Sample	% Cal	AR	RMS (μm)	σ (MPa) Barnhoorn et al. (2004)	$\dot{\varepsilon}$ (GBM) (s^{-1}) (T=400-500°C)	Mean twin width (μm)	Mean twin density (n/mm)	σ_{twin} (MPa) Rybacki et al. (2011)	$\dot{\varepsilon}$ (twin) (s^{-1}) (T=250°C)
K21-10-12A	65	2.24	250±30	13.7±4.8	3.1E-11	-	-	-	-
K21-10-12	65	2.45	390±180	10.2±3.6	1.7E-11	3±1	43	128±8	5.0E-15
K22-10-19	80	1.98	530±170	8.3±2.9	1.1E-11	3±1	48	135±9	9.4E-15
K29-10-51	78	1.96	490±160	8.7±3.1	1.4E-09	-	-	-	-
K29-10-52	73	2.13	440±140	9.4±3.3	1.6E-09	2±1	55	145±9	2.2E-14
K31-10-64	70	2.48	710±150	6.8±2.4	8.1E-10	4±1	42	126±8	4.4E-15
K31-10-65	75	2.41	770±200	-	-	-	-	-	-

Table 2 – Results from grain size and twin analyses. %Cal = abundance of calcite in sample; AR = aspect ratio; RMS= root mean square calcite crystal equivalent diameter; σ (MPa) Barnhoorn et al. (2004) = differential stress calculated from the RMS. $\dot{\varepsilon}$(GBM) = strain rate from dynamic recrystallization mechanisms (Renner et al., 2002). σ_{twin} (MPa) = differential stress based on the twin density from Rybacki et al. (2011) paleopiezometer. $\dot{\varepsilon}$ (twin) = strain rate from Rutter (1974).

Table 3

Sample	Rxz	δ° (Sb angle)	simple shear %	Wn (Sb)	S (Rxz, Sb)	ω° CPO	simple shear % (CPO)	Wm (CPO)	S (Rxz, [*c*]-axis)
K21-10-12A	1.242	*ND*	*ND*	*ND*	*ND*	*ND*	*ND*	*ND*	*ND*
K21-10-12	1.322	20	41	0.64	0.92	2	5	0.08	0.87
K21-10-13	1.270	23	46	0.72	0.91	*ND*	*ND*	*ND*	*ND*
K22-10-18	*ND*	*ND*	*ND*	*ND*	*ND*	10	30	0.45	0.86
K22-10-19	1.403	25	49	0.77	0.90	10	30	0.45	0.86
K29-10-52	1.463	26	50	0.79	0.89	15	50	0.71	0.87

Table 3 – Results from finite-strain and CPO analyses. Rxz = Axial ratios from the ellipse voids (Waldron and Wallace, 2007); δ°= angle between the oblique foliation (Sb) and the main foliation (Sp); ω° = angle between the main [c]-axes orientation and the plane normal to the foliation; Wn = sectional vorticity number; Wm = mean kinematic vorticity number; S = shortening.